

Stability-Aware Training of Neural Network Interatomic Potentials with Differentiable Boltzmann Estimators

Sanjeev Raja¹, Ishan Amin^{1,2}, Fabian Pedregosa³, and Aditi S. Krishnapriyan^{a4, 1}

¹Department of Electrical Engineering and Computer Science, University of California, Berkeley

²Department of Physics, University of California, Berkeley

³Google DeepMind

⁴Department of Chemical and Biomolecular Engineering, University of California, Berkeley

Abstract

Neural network interatomic potentials (NNIPs) are an attractive alternative to *ab-initio* methods for molecular dynamics (MD) simulations. However, they can produce unstable simulations which sample unphysical states, limiting their usefulness for modeling phenomena occurring over longer timescales. To address these challenges, we present Stability-Aware Boltzmann Estimator (StABIE) Training, a multi-modal training procedure which combines conventional supervised training from quantum-mechanical energies and forces with reference system observables, to produce stable and accurate NNIPs. StABIE Training iteratively runs MD simulations to seek out unstable regions, and corrects the instabilities via supervision with a reference observable. The training procedure is enabled by the Boltzmann Estimator, which allows efficient computation of gradients required to train neural networks to system observables, and can detect both global and local instabilities. We demonstrate our methodology across organic molecules, tetrapeptides, and condensed phase systems, along with using three modern NNIP architectures. In all three cases, StABIE-trained models achieve significant improvements in simulation stability and recovery of structural and dynamic observables. In some cases, StABIE-trained models outperform conventional models trained on datasets 50 times larger. As a general framework applicable across NNIP architectures and systems, StABIE Training is a powerful tool for training stable and accurate NNIPs, particularly in the absence of large reference datasets.

Molecular dynamics (MD) simulation is a staple method of computational science, enabling high-resolution spatiotemporal modeling of atomistic systems throughout biology, chemistry, and materials science [21]. Under the Born-Oppenheimer approximation, system evolution is governed by the underlying potential energy surface (PES), which is a function of the nuclear Cartesian coordinates [11]. While the atomic forces needed for MD simulation can be obtained on-the-fly via *ab-initio* quantum-mechanical (QM) calculations [12], the unfavorable scaling of this approach makes it prohibitively expensive for realistic system sizes and timescales [22].

There is a long history of using machine learning (ML) approaches in place of *ab-initio* methods to efficiently approximate the global PES [7, 6, 2, 55]. Neural network interatomic potentials (NNIP) have recently emerged as a highly successful class of ML methods, demonstrating the ability to capture complex many-body interactions, and in some cases transfer flexibly across chemical space [58, 29, 42, 24, 25, 5, 47,

^aCorresponding author: aditik1@berkeley.edu

4, 59]. NNIPs, typically parameterized as graph neural networks [56, 33], are trained by matching energy and forces of a molecule or material from a reference dataset of QM calculations, such as Density Functional Theory (DFT) [31]. NNIPs trained on large *ab-initio* datasets are increasingly being used to model challenging and important chemical systems with favorable results [45, 37, 15, 57, 64, 43, 14, 3, 36, 60, 26, 19].

MD simulations aim to accurately estimate system observables like the radial distribution function, virial stress tensor, and diffusivity coefficient. This often requires long simulation to fully explore the underlying PES and minimize sampling error. Unfortunately, NNIPs are known to produce unstable simulations, meaning that they can irreversibly enter unphysical regions of phase space (e.g., a bond breaking event in a non-reactive system at low temperature) [23, 63, 69, 8, 46, 72]. Sampling of such regions often quickly leads to unrecoverable simulation collapse as the NNIP drifts far from the distribution of its training data. As a result, computed observables may have high statistical error due to insufficient sampling, or be altogether inaccurate. This can limit the ability of NNIP-based MD simulations to investigate long-timescale phenomena like ion diffusion and protein folding, as well as rare events that may require extensive sampling to encounter. Figure 1 illustrates typical NNIP instability behaviors and provides examples of unstable structures sampled during MD simulation.

Insufficient coverage of phase space and inaccuracies within the reference datasets utilized for training NNIPs have been suggested as factors contributing to instability [23, 63, 69, 8, 46, 72]. Expanding the dataset requires additional QM calculations, and improving its accuracy requires more exact QM approaches [39]. Both options are very computationally expensive, particularly for larger systems like macromolecules. Recent work has even suggested that expanding the dataset may not always improve stability [23], consistent with the notion that phase space is sampled with exponentially vanishing probability based on the local potential energy. This suggests the need for additional sources of information beyond energies and forces to train stable NNIPs.

We posit that system observables derived from experiment or high-fidelity simulation can serve this purpose. Parameterizing NNIPs to match observables is an alternative approach to conventional energy-and-forces-training [65, 70]. This approach has been successful in learning potentials of condensed-phase [71] and titanium [54] systems, enhanced sampling of rare events [61], and protein folding simulation [30, 48, 34]. However, using observables to improve the stability of NNIPs in downstream MD simulations remains unexplored.

In this work, we introduce **Stability-Aware Boltzmann Estimator (StABIE) Training**, a procedure designed to produce NNIPs that are both stable and accurate. The core idea behind StABIE is to use MD simulation to rapidly explore regions of molecular phase space where the NNIP becomes unstable, followed by a targeted refinement of these regions using reference system observables. The key to efficient and numerically stable training lies in the Boltzmann Estimator, which avoids computing gradients directly through MD simulations. StABIE Training is a self-contained, efficient process that leverages learning signals from both reference observables and existing QM data, with no reliance on performing additional QM reference calculations. To our knowledge, StABIE Training is the first method that combines these data modalities to improve the stability of neural network potentials in MD simulations. Its flexibility allows for integration with any NNIP architecture or molecular system, making it a valuable addition to existing NNIP workflows.

We demonstrate StABIE Training on three systems and NNIP architectures: 1) simulation of aspirin with SchNet [58], 2) simulation of the Ac-Ala3-NHMe tetrapeptide with NequIP [5], and 3) simulation of an

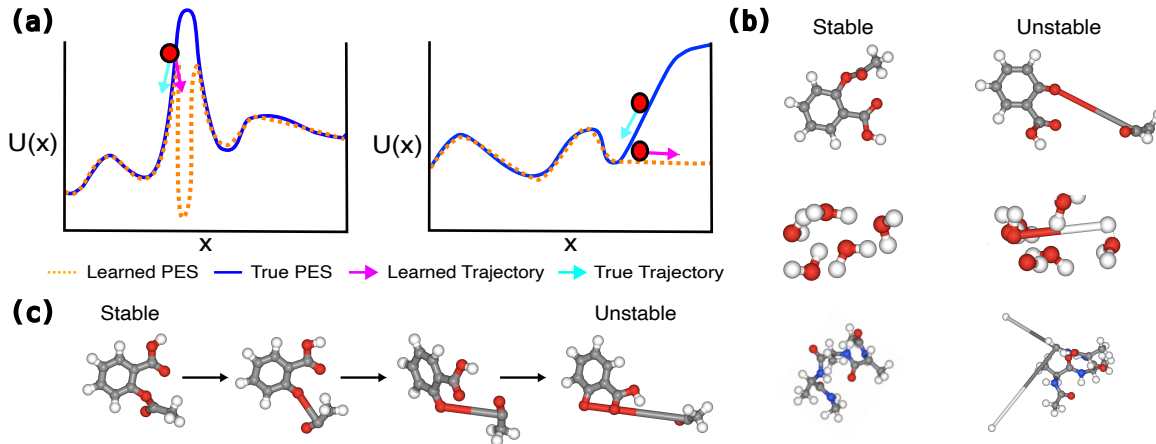


Figure 1: Neural network interatomic potential (NNIP) failure modes. (a) Illustrative examples of true and learned potential energy surfaces (PES) and resulting dynamics for unstable NNIPs. NNIPs can be highly accurate in approximating most of the PES, but contain localized "holes" where energy and forces estimates deviate significantly from the true PES, leading to sampling of highly unphysical regimes. Once such a regime is reached, further simulation typically does not re-enter physically plausible regions. As a result, observables computed from MD simulation may be inaccurate or have high statistical error. (b) Examples of stable versus unstable configurations sampled by NNIPs during molecular dynamics simulation of systems considered in this work. The unstable configurations contain unphysical bond lengths, angles, and coordination structures which are not meaningful for observable calculations. (c) Selected states from an unstable MD trajectory of aspirin. A unidirectional progression is demonstrated, in which a stable, physical configuration evolves into a highly unstable, unphysical configuration.

all-atom water system with GemNet-T [24]. Relative to NNIPs trained solely on reference energy and forces data, our StABIE-trained models produce significantly more stable downstream MD simulations and recover both structural and dynamical observables more accurately. For an aspirin simulation with a SchNet model trained on 1,000 reference structures, StABIE Training increases the median stability from 35 to 140 picoseconds, exhibits better generalization to unseen simulation temperatures, and outperforms models trained on 50 times larger, labeled datasets. For an all-atom water simulation with a GemNet-T model trained on 1,000 reference structures, StABIE Training improves the median stability from 23 to 52 picoseconds and yields an 87% accuracy improvement in estimation of the diffusivity coefficient. Our results suggest that utilizing both quantum-mechanical and observable-based modalities is required to fully exploit the available learning signal in reference datasets and train stable and accurate NNIPs.

1 Preliminaries

Molecular Dynamics. Molecular dynamics simulation is used to evolve the positions and momenta of an atomistic system. Consider a system of N atoms. The state of the system at time t is defined by $\Gamma(t) = \{r(t), p(t)\}$, where $r(t), p(t) \in \mathbb{R}^{N \times 3}$ are the position and momenta of the atoms. We assume the system has a scalar-valued Hamiltonian function $\mathcal{H} : \mathbb{R}^{N \times 3} \times \mathbb{R}^{N \times 3} \rightarrow \mathbb{R}$ of the form,

$$\mathcal{H}(\Gamma) = \sum_{i=1}^N \frac{p_i^2}{2m_i} + U(r), \quad (1)$$

where $U : \mathbb{R}^{N \times 3} \rightarrow \mathbb{R}$ is a potential energy function and m_i and p_i are the mass and momentum of atom i . The system obeys Hamilton's laws of motion,

$$\dot{r}_i = \frac{\partial H}{\partial p_i} = \frac{p_i}{m_i}, \quad \dot{p}_i = -\frac{\partial H}{\partial r_i} = -\frac{\partial U(r_i)}{\partial r_i}. \quad (2)$$

Evolving these equations in time for T_f steps produces a sequence of simulation states, $\bar{\Gamma} = \{\Gamma(t)\}_{t=0}^{T_f}$, which conserve the Hamiltonian and constitute samples from the microcanonical ensemble. It is also common to couple a thermostat to the simulation to conserve temperature instead of the Hamiltonian, thereby sampling from the canonical ensemble. In this case, the state distribution has a Boltzmann form: $P(\Gamma) \propto e^{-\frac{H(\Gamma)}{k_B T}}$ where T is the temperature and k_B is Boltzmann’s constant.

Training Neural Network Potentials with Reference Energies and Forces. In the context of neural network interatomic potentials (NNIPs), the potential energy is approximated by a function U_θ with learnable parameters θ given by a neural network. When training a model to learn from quantum mechanical reference data, θ is obtained by using stochastic gradient descent (SGD) to minimize the following energy and forces loss function:

$$\mathcal{L}_{\text{QM}}(\theta) \stackrel{\text{def}}{=} \mathbb{E}_{\Gamma \sim P_{\text{QM}}(\Gamma)} \left[\lambda_U \|U_{\text{ref}}(\Gamma) - U_\theta(\Gamma)\|_2^2 + \lambda_F \|F_{\text{ref}}(\Gamma) + \nabla_r U_\theta(\Gamma)\|_2^2 \right], \quad (3)$$

where $P_{\text{QM}}(\Gamma)$ is the equilibrium distribution induced by *ab-initio* (or high-fidelity) simulation, U_{ref} and F_{ref} are the high-fidelity reference energy and force functions, and λ_U and λ_F are hyperparameters controlling the relative weights of the energy and force loss terms. Note that while we have adopted the notation $U(\Gamma)$ for convenience, the potential energy is a function only of the position component, r , of the state Γ . In this work, $P_{\text{QM}}(\Gamma)$ is approximated by a reference dataset $\mathcal{D}_{\text{train}}$ of states sampled from a high-fidelity simulation, such as *ab-initio* molecular dynamics. We note that in some cases, $\mathcal{D}_{\text{train}}$ may not be fully representative of $P_{\text{QM}}(\Gamma)$, due to biased sampling procedures favoring rare or interesting events.

Estimation of System Observables from MD Simulation. Observables, $g(\Gamma(t))$, characterize the state of a MD simulation at time t , and relate to macroscopic properties or experimental measurements of the system. Examples include the radial and angular distribution functions, velocity autocorrelation function, and diffusivity coefficient. Observables can be computed conveniently as an empirical average over states from a MD simulation. This is justified by the ergodicity hypothesis, under which a time-average over a sufficiently long simulation converges to a distributional average over the Boltzmann distribution. For more detail on the observables used in this work, please refer to Supplementary Section A.4.

2 Methods

We present StABIE Training, our proposed procedure to train stable and accurate NNIPs by leveraging both reference quantum mechanical data and system observables. Our approach is enabled by Boltzmann Estimators, which allows gradient-based optimization of NNIPs based on system observables.

2.1 Boltzmann Estimator

Reference system observables can be estimated from high-fidelity MD simulations or experimental measurements. Since observables are linked to the NNIP parameters through a molecular simulation, training with this source of information requires a reliable way to optimize through MD trajectories.

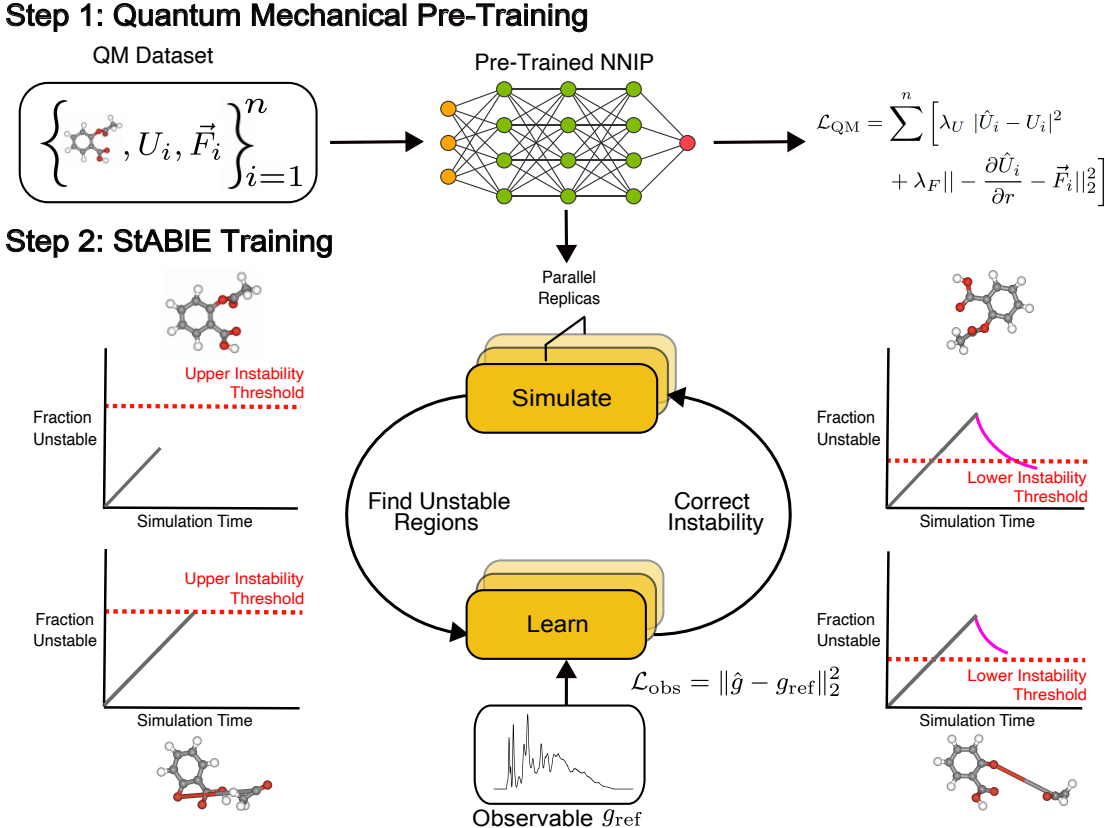


Figure 2: Schematic of Stability-Aware Boltzmann Estimator (StABIE) Training procedure. Our proposed StABIE Training procedure begins with conventional pre-training on a small reference dataset of QM calculations (in the loss, \hat{U} refers to the NNIP-predicted energy). This dataset remains fixed throughout the procedure, and is never expanded with new calculations. Upon convergence of pre-training, StABIE then alternates between two main phases, simulation and learning. In the simulation phase, we perform many molecular dynamics simulations in parallel with the NNIP and find regions of instability. When a sufficient fraction of simulations become unstable, we enter the learning phase, where the NNIP is further trained to match known system observables from *ab-initio* simulation or experiment (in the loss, \hat{g} refers to the NNIP-predicted observable). After a sufficient reduction in the portion of unstable trajectories, we re-enter the simulation phase, and repeat the training cycle until a predetermined computational budget is reached. Sample stable and unstable molecules are included next to the corresponding graphs.

Formally, we define $g(\Gamma)$ to be a vector-valued observable of a state Γ , and g_{ref} to be the reference value of the observable. To train our NNIP with information about the system observable, we seek to minimize the following loss function:

$$\mathcal{L}_{\text{obs}}(\theta) \stackrel{\text{def}}{=} \|\mathbb{E}_{\Gamma \sim P_{\theta}(\Gamma)}[g(\Gamma)] - g_{\text{ref}}\|_2^2, \quad (4)$$

where $P_{\theta}(\Gamma)$ is the equilibrium distribution induced by the NNIP U_{θ} . In this work, we consider systems with a fixed volume, temperature, and number of particles, corresponding to the canonical ensemble. This means that microstates obey a Boltzmann distribution, $P_{\theta}(\Gamma) = \exp\left(-\frac{1}{k_B T} \mathcal{H}_{\theta}(\Gamma)\right) / C(\theta)$, where the Hamiltonian

$\mathcal{H}_\theta(\Gamma) = \sum_{i=1}^N \frac{p_i^2}{2m_i} + U_\theta(\Gamma)$, T is the sampling temperature, k_B is Boltzmann’s constant, and $C(\theta) = \int \exp(-\frac{1}{k_B T} \mathcal{H}_\theta(\Gamma')) d\Gamma'$ is the normalizing partition function. MD simulation is required at each training iteration to sample from this distribution and estimate the loss.

We optimize the parameters of the NNIP, θ , using stochastic gradient descent. This requires computing gradients of Equation 4 with respect to θ . The required gradient, $\nabla_\theta \mathcal{L}_{\text{obs}}$, can be decomposed via the chain rule as follows:

$$\begin{aligned} \nabla_\theta \mathcal{L}_{\text{obs}}^\top &= \frac{\partial \mathcal{L}_{\text{obs}}}{\partial \mathbb{E}_{\Gamma \sim P_\theta(\Gamma)}[g(\Gamma)]} \frac{\partial \mathbb{E}_{\Gamma \sim P_\theta(\Gamma)}[g(\Gamma)]}{\partial \theta} \\ &= 2(\mathbb{E}_{\Gamma \sim P_\theta(\Gamma)}[g(\Gamma)] - g_{\text{ref}})^\top \frac{\partial \mathbb{E}_{\Gamma \sim P_\theta(\Gamma)}[g(\Gamma)]}{\partial \theta}. \end{aligned} \quad (5)$$

The non-trivial quantity to compute is the Jacobian, $\partial \mathbb{E}_{\Gamma \sim P_\theta(\Gamma)}[g(\Gamma)]/\partial \theta$. One way to estimate this quantity is by using a chain rule expansion that corresponds to each step of the unrolled MD simulation [70]. However, this approach is memory-intensive and can lead to numerical instability for long trajectories [71, 61]. We can instead leverage the known Boltzmann form of the state distribution to construct an unbiased estimator of the Jacobian.

Definition 1 (*N*-sample Boltzmann estimator). *Given N independent samples $\Gamma^{(1)}, \dots, \Gamma^{(N)}$ from a Boltzmann distribution $P_\theta(\Gamma)$, we define the N -sample Boltzmann estimator $\mathcal{E}(\Gamma^{(1)}, \dots, \Gamma^{(N)})$ as,*

$$\begin{aligned} \mathcal{E}(\Gamma^{(1)}, \dots, \Gamma^{(N)}) &= \\ &= \frac{N}{k_B T(N-1)} \left[\hat{\mathbb{E}}[g(\Gamma)] \hat{\mathbb{E}}[\nabla_\theta U_\theta(\Gamma)]^\top - \hat{\mathbb{E}}[g(\Gamma) \cdot \nabla_\theta U_\theta(\Gamma)^\top] \right], \end{aligned} \quad (6)$$

where $\hat{\mathbb{E}}[f(\Gamma)] = \frac{1}{N} \sum_{i=1}^N f(\Gamma^{(i)})$ denotes an empirical mean over the samples.

This estimator provides an unbiased estimate of the Jacobian $\frac{\partial \mathbb{E}_{\Gamma \sim P_\theta(\Gamma)}[g(\Gamma)]}{\partial \theta}$. Our proof is provided in Supplementary Section A.1. This result can also be derived using thermodynamic perturbation theory [74, 65].

Localized Boltzmann Estimator for Spatial Specificity. In some scenarios, unphysical configurations can occur within localized regions of the simulation domain, such as collisions between two molecules in a large condensed-phase system. Due to spatial averaging, global observables $g(\Gamma)$ may be insensitive to these localized events, limiting the ability to identify unphysical states. To address this, we propose the N -sample Localized Boltzmann Estimator. Here, the global energy $U_\theta(\Gamma)$ and observable $g(\Gamma)$ are replaced with local versions $U_\theta(\gamma)$ and $g(\gamma)$, where γ denotes a local neighborhood of $n < N$ atoms. NNIPs compute global energies by summing individual atomic energies, and we can leverage this to compute $U_\theta(\gamma)$ by summing only over atoms in the local neighborhood. See Supplementary Section A.2 for a formal definition of the localized estimator. A concrete example of localized instability, along with the use of our localized Boltzmann estimator to correct it, will be presented in the context of an all-atom water system in Results, Section 3.4.

Key Advantages. The Boltzmann estimators defined earlier have several advantages over explicit differentiation through the MD simulation to train the NNIP. Due to the use of independent samples, the estimator avoids numerical instability associated with differentiating through long, continuous trajectories. Further, the most computationally expensive component of the estimator, the gradient of the potential energy

$\nabla_{\theta}U_{\theta}(\Gamma)$, is independent of the observable $g(\Gamma)$. This means it can be reused, allowing efficient training to match multiple observables simultaneously. Finally, our localized formulation of the estimator enables finer control over isolated instabilities, providing a more informative gradient with which to optimize the NNIP.

2.2 Stability-Aware Boltzmann Estimator (StABIE) Training

Stability-Aware Boltzmann Estimator (StABIE) Training begins with conventional supervised pre-training of a NNIP on a dataset of structures from a high-fidelity, constant temperature MD simulation, paired with reference energy and forces values. The method then proceeds by alternating between two major phases, simulation and learning, as illustrated in Figure 2.

Simulation Phase. The simulation phase aims to explore the molecular phase space and pinpoint regions where the NNIP becomes unstable. We sample R equilibrium states from the training dataset as initial conditions for separate MD trajectories (replicas). Using the pre-trained NNIP U_{θ} , we run MD simulations on these replicas in parallel for t timesteps. We apply a predetermined stability criterion (see Supplementary Section A.5 for details) to each replica, freezing those marked unstable at their current states. Simulations continue for the remaining replicas, with stability checks every t timesteps. Once a specified fraction of replicas become unstable, we rewind all unstable replicas by t timesteps. This ensures that further simulation for t timesteps will trigger instability, which is then corrected in the next phase.

Learning Phase. The learning phase aims to refine the NNIP to correct the previously encountered instabilities. Starting from the near-unstable configurations obtained in the simulation phase, we perform MD simulation for t timesteps, sampling every S^{th} state to obtain uncorrelated samples. Using the sampled states $\Gamma^{(1)}, \dots, \Gamma^{(N_d)}$, where $N_d = \frac{t}{S}$, we compute the observable loss function (Equation 4). To update the NNIP parameters θ , we compute an unbiased estimator of the loss gradient via the Boltzmann Estimator (Section 2.1) and use it to perform a single step of gradient descent. We then reset all replicas to their original near-unstable states, simulate with the updated NNIP, recompute the loss and gradient estimator with the newly sampled states, and again update the NNIP weights. This process is repeated until the fraction of unstable replicas drops below a predetermined threshold. When this occurs, the learning phase has concluded, and we begin a new simulation phase starting from the endpoints of the last learning phase. We continue alternating between simulation and learning phases until a predetermined computational budget is reached, at which point StABIE Training has concluded. See Supplementary Section A.3 for a formal algorithmic description of the StABIE Training procedure.

Regularizing StABIE Training with Energy and Forces Reference Data. In practice, the mapping between a sparse set of system observables and a potential energy function is non-unique [50]. Consequently, learning with observables alone is underconstrained. To combat this, we regularize the observable loss function (Equation 4) with the energy and forces loss function (Equation 3). The final StABIE loss function thus becomes,

$$\mathcal{L}_{\text{StABIE}}(\theta) \stackrel{\text{def}}{=} \mathcal{L}_{\text{obs}} + \lambda \mathcal{L}_{\text{QM}}, \tag{7}$$

where \mathcal{L}_{obs} and \mathcal{L}_{QM} were defined in Equations 4 and 3 respectively, and the hyperparameter λ controls the strength of the regularization. Crucially, \mathcal{L}_{QM} is still only computed over the static training dataset $\mathcal{D}_{\text{train}}$, and not over new structures explored during MD simulation. Therefore, the regularization introduces no additional quantum-mechanical supervision.

3 Results

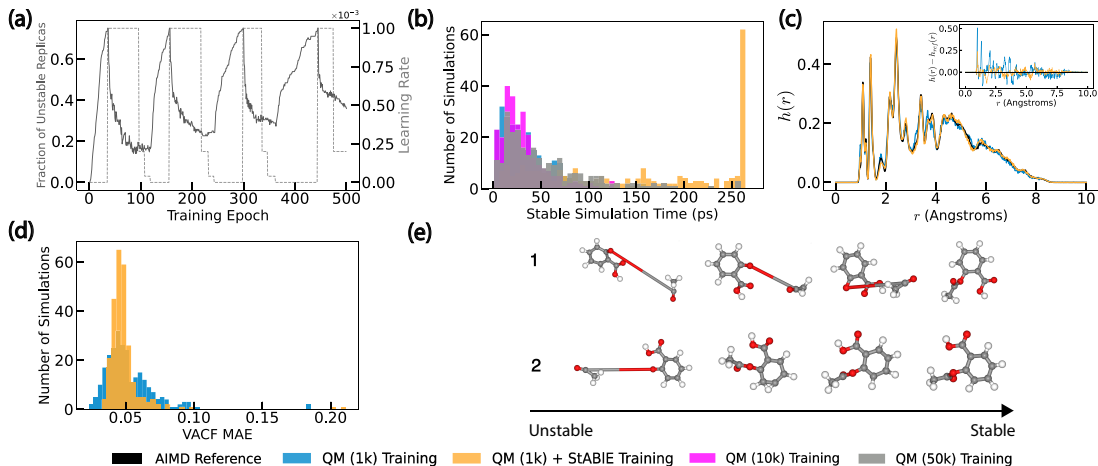


Figure 3: Aspirin simulation with StABIE Training. Results of StABIE Training a SchNet [58] NNIP on the 21-atom aspirin molecule from the MD17 [18] dataset at 500 Kelvin. (a) Alternation of simulation and learning phases during StABIE Training with 128 parallel replicas. The simulation phases correspond to regions where no learning occurs and the fraction of unstable replicas increases, while the learning phases correspond to regions where learning occurs and the fraction of unstable replicas decreases. (b) Stable simulation time of 256 parallel aspirin trajectories from a SchNet NNIP trained on 1,000 (blue), 10,000 (magenta), 50,000 (grey) quantum mechanical (QM) energy and forces reference data points. We apply StABIE Training on the SchNet NNIP trained with 1,000 QM data points. This results in significantly more stable simulations (orange), surpassing models trained on $50\times$ more QM data. (c) Distribution of interatomic distances ($h(r)$) from an *ab-initio* molecular dynamics (AIMD) simulation (black), a SchNet model trained on 1,000 QM data points (blue), and a SchNet model trained on 1,000 QM data points, followed by our StABIE Training procedure (orange). A StABIE-trained SchNet model closely recovers the true distribution of interatomic distances, while the model trained only on QM reference data produces a noisier $h(r)$ because it cannot stably simulate the system for longer time periods. Inset shows difference between predicted and reference $h(r)$. (d) Distribution of velocity autocorrelation function (VACF) mean absolute error (MAE) relative to an *ab-initio* simulation from a SchNet model trained on 1,000 QM data points (blue) and a SchNet model trained on 1,000 QM datapoints, followed by our StABIE Training procedure (orange). The VACF is an observable computed from simulation dynamics, which the model is not trained on. While the mean accuracy of the StABIE-trained SchNet model is similar to the QM-only baseline, there is a reduction in variance across replicas. (e) Aspirin structures sampled over epochs of a single learning phase of StABIE Training. There is a clear progression as unstable configurations become stable.

We present the results of our StABIE training procedure on three different systems and NNIP architectures: 1) an aspirin molecule with a SchNet [58] architecture (Sections 3.1 - 3.2), 2) an Ac-Ala3-NHMe tetrapeptide with a NequIP [5] architecture (Section 3.3), and 3) an all-atom water system with a GemNet-T [24] architecture (Section 3.4). For systems 1) and 2), we use the Boltzmann estimator presented in Equation 6. For system 3), we employ our localized Boltzmann estimator (Equation 8) to correct isolated instabilities. We focus our evaluation of NNIPs on their ability to produce stable MD simulations which accurately recover key system observables. For all systems, stability thresholds are chosen to be very large relative to the scale of typical fluctuations in reference simulations at the chosen temperature. Simulations which cross the threshold thus cannot reasonably re-enter the manifold of stable configurations (see Supplementary Section A.5 for more details). We compute simulation observables by averaging over sampled states from the trajectory corresponding to the median stability improvement (over all replicas) between the baseline and StABIE-trained NNIP. More detailed information about NNIP architectures, training, simulation, and evaluation can be found in Supplementary Sections A.6, A.7, and A.8.

3.1 Aspirin Molecule

Aspirin (chemical formula $C_9H_8O_4$) is the largest molecule from MD17 [18], a widely used benchmark dataset for atomistic simulations which contains energy and forces calculations computed at the PBE+vdW-TS [66] level of theory. Consisting of 21 atoms, aspirin has been shown to be the most challenging molecule in MD17 for state-of-the-art NNIPs to simulate stably [23].

Problem setup. We pre-train a SchNet [58] model on the energy and forces matching objective (Equation 3) using a subset of 1,000 aspirin structures from the reference dataset. After convergence, we begin StABIE Training with the global Boltzmann estimator, using 128 parallel replicas at a temperature of 500K. By simulating hundreds of replicas in parallel, we expose the NNIP to a comprehensive range of failure modes much more quickly than possible with a single replica. Following [23], we use a maximum bond length deviation criterion to detect instability in the simulations (see Supplementary Section A.5 for details). We use the distribution of interatomic distances, $h(r)$, as our training observable, with the $h(r)$ computed over structures in the training dataset serving as the reference (see Supplementary Section A.4 for details). This choice is motivated by the observation that unphysical bond stretches constitute the majority of failure cases in aspirin simulations. The $h(r)$ is sensitive to these abnormalities, and is thus an informative optimization criterion. We perform four complete StABIE cycles of simulation and learning with a SGD optimizer.

Results. We evaluate our final models by performing constant-temperature MD simulations, starting from 256 initial structures not seen during training. Figure 3a shows the progression of StABIE Training. During the simulation phase, the learning rate is zero and the fraction of unstable replicas steadily increases. When the upper instability threshold is reached, learning commences. The fraction of unstable replicas steadily decreases, confirming that optimization of the interatomic distance distribution produces the desired stability improvement. A decaying learning rate schedule is employed to avoid overfitting to the current batch of replicas.

A SchNet model trained via our stability-aware approach is significantly more stable during MD simulation than models trained only on the conventional QM energy and forces objective function (Figure 3b). As a result of our training procedure, the mean stable simulation time increases from 35 to 140 picoseconds. Even when StABIE training is employed after training on only on 1,000 reference structures, it is more stable than models trained conventionally on 10,000 and 50,000 reference structures, highlighting the effectiveness of our method in improving stability without reliance on any additional QM reference data. We also observe that simply reducing the simulation timestep does not reliably lead to an improvement in the stability of simulations produced by conventionally trained models (see Supplementary Section A.11 for details).

Simulations from our model closely recover the true distribution of interatomic distances, while the distributions produced by models solely trained on QM data are noisier, due to the limited stable simulation time (Figure 3c). We also test the ability of our StABIE-trained model to recover the velocity autocorrelation function (VACF), a fundamental dynamical observable not seen during training (Figure 33). We see that the quality of the recovered VACF remains similar after StABIE Training, with lower variance over the simulated replicas (see Supplementary Section A.12 for a sample VACF computed from the simulations). The preservation of a held-out dynamical observable suggests that StABIE Training does not achieve stability improvements by simply restricting the model around a narrow regime corresponding to the reference $h(r)$. If this were the case, characteristic dynamic fluctuations around the reference $h(r)$ would be suppressed, leading to an inaccurate VACF. Figure 3e depicts aspirin structures sampled from simulations during the

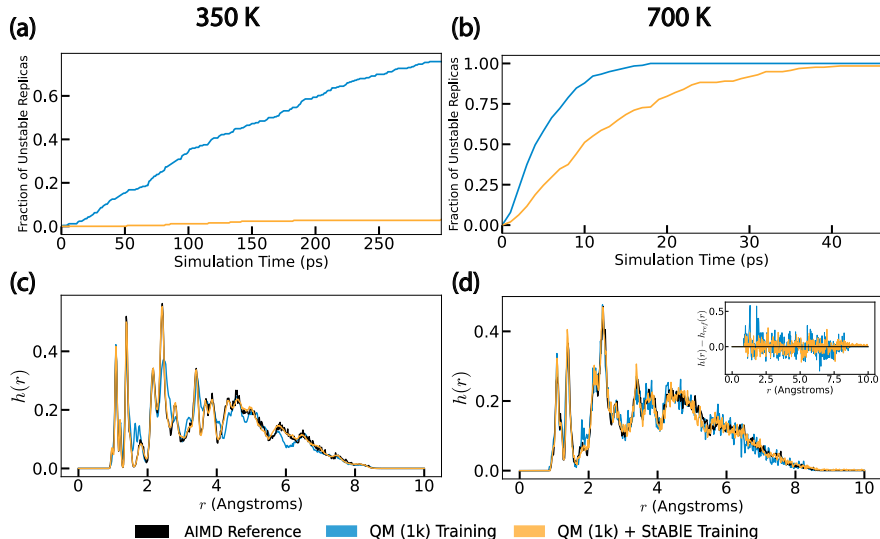


Figure 4: Testing temperature generalization for aspirin. We test the generalization of StABIE Training by performing 256 parallel MD simulations at 350 Kelvin and 700 Kelvin with a SchNet model which was StABIE-trained at 500 Kelvin on aspirin from MD17. **(a, b)** Fraction of unstable replicas as a function of simulation time for a SchNet NNIP trained on 1,000 mechanical (QM) energy and forces reference data points (blue). Applying StABIE Training to this model yields significantly more stable simulations (orange). At 350K, before StABIE Training, 70% of replicas are unstable after 300 picoseconds of simulation. After StABIE Training, <5% of replicas are unstable. **(c, d)** Distribution of interatomic distances ($h(r)$) from an *ab-initio* molecular dynamics (AIMD) simulation (black), a SchNet model trained on 1,000 QM data points (blue), and a SchNet model trained on 1,000 QM datapoints, followed by our StABIE Training procedure (orange). The StABIE-trained SchNet model more accurately recovers the true $h(r)$ at both 350K and 700K. At 350K, the baseline model trained only on QM data incorrectly estimates several peaks in the $h(r)$, while at 700K the baseline model produces a noisy $h(r)$ due to its limited stable simulation time (inset shows difference between the predicted and reference $h(r)$). The AIMD reference $h(r)$ is computed by Boltzmann-reweighting of independent samples from the 500K training dataset.

course of a single learning phase of StABIE Training, demonstrating that unphysical bond stretching in these structures is resolved by the training procedure.

3.2 Temperature generalization

Problem setup. We explore our method’s generalization to different thermodynamic conditions. To do so, we perform 256 parallel MD simulations at 350K and 700K using the SchNet model which was trained with our StABIE Training procedure at 500K. We use the same criterion based on bond length deviation to detect instability as in Section 3.1. We estimate the reference $h(r)$ at 350K and 700K by Boltzmann-reweighting samples from the original 500K training dataset (see Supplementary Section A.9 for details).

Results. Aspirin simulations produced by a StABIE-Trained SchNet model are significantly more stable at both temperatures than baseline models trained only on QM reference data (Figure 4a, b). At 350K, the difference is particularly large. After 300 picoseconds of simulation, less than 5% of replicas are unstable in the StABIE-trained NNIP simulation, while over 75% replicas are unstable in the baseline NNIP simulation. The StABIE-trained model also recovers the true distribution of interatomic distances more closely than the baseline NNIP at both temperatures (Figure 4c, d). At 350K, the baseline NNIP is stable enough produce

a smooth $h(r)$, but the structure is inaccurate, indicating incorrect sampling of the phase space. At 700K, the baseline NNIP produces a $h(r)$ which is close to the AIMD-produced distribution, but is noisy due to insufficient stable simulation time. This underscores the necessity for a NNIP to be both stable and accurate in order to be practically useful in MD simulation. StABIE Training improves both of these metrics for this system. As generalization to new thermodynamic conditions is of crucial importance for NNIPs to be useful in practical applications [35], we see the temperature-transferability of StABIE Training as an important strength of our method.

3.3 Ac-Ala3-NHMe Tetrapeptide

Ac-Ala3-NHMe (chemical formula $C_{12}H_{22}N_4O_4$) is a tetrapeptide from the MD22 dataset [17], a challenging benchmark consisting of reference energy and forces computed at the PBE+MBD [51, 67] level of theory for considerably larger molecules than those in the MD17 dataset. Relative to MD17 molecules, Ac-Ala3-NHMe poses unique challenges for atomistic simulations due to its larger size and flexibility [32]. As a result, more expressive NNIPs—often incorporating E(3) equivariance [27]—are required to accurately model the underlying potential energy surface.

Problem setup. In our experiments, we use a NequIP [5] model due to its promising accuracy and data efficiency on challenging atomistic simulation tasks [37, 45]. We pre-train a NequIP model on the QM energy and forces matching objective using 14,890 (or 25%) of available structures from the training dataset. After convergence, we begin StABIE Training with the global Boltzmann estimator, using 48 parallel replicas at a temperature of 500K. As with aspirin (Sections 3.1 - 3.2), we detect instability using the maximum bond length deviation criterion, and choose the distribution of interatomic distances, $h(r)$, as our training observable.

Results. The StABIE-trained NequIP model gives an improvement in stability relative to a baseline model trained only on QM reference data (Figure 5a). Additionally, the StABIE-trained model closely recovers the true $h(r)$, while the baseline NNIP produces a highly noisy $h(r)$. This is because of insufficient sampling, due to a lower stable simulation time (Figure 5b). The baseline NNIP also underestimates the latter portion of the $h(r)$ distribution, indicating poor modelling of long-range interactions. Figure 5c shows selected structures throughout the course of a single learning phase of StABIE Training, demonstrating a progression from very unstable to stable structures.

3.4 Water

As a final evaluation of StABIE Training, we consider liquid-phase water. Water has historically posed unique challenges for atomistic simulations due to the presence of long-range interactions, proton disorder, and nuclear quantum effects [16, 52, 44]. Additionally, estimating transport properties, such as the diffusivity coefficient, requires long, continuous trajectories to minimize statistical error. We use the dataset produced in [23], which contains reference all-atom simulations of 64 water molecules using the flexible Extended Simple Point Charge model [73] at 300K and 1 atm. For this system, we consider a GemNet-T model [24]. GemNet-T displays a failure mode in which unphysical configurations (e.g., bond stretching) first arise in highly localized "pockets" of 1-2 molecules (Figure 6a), which then gradually cascade to the rest of the simulation domain [23]. Such configurations do not noticeably affect global system observables such as the radial distribution function. Therefore, in this setting it is more appropriate to use our localized

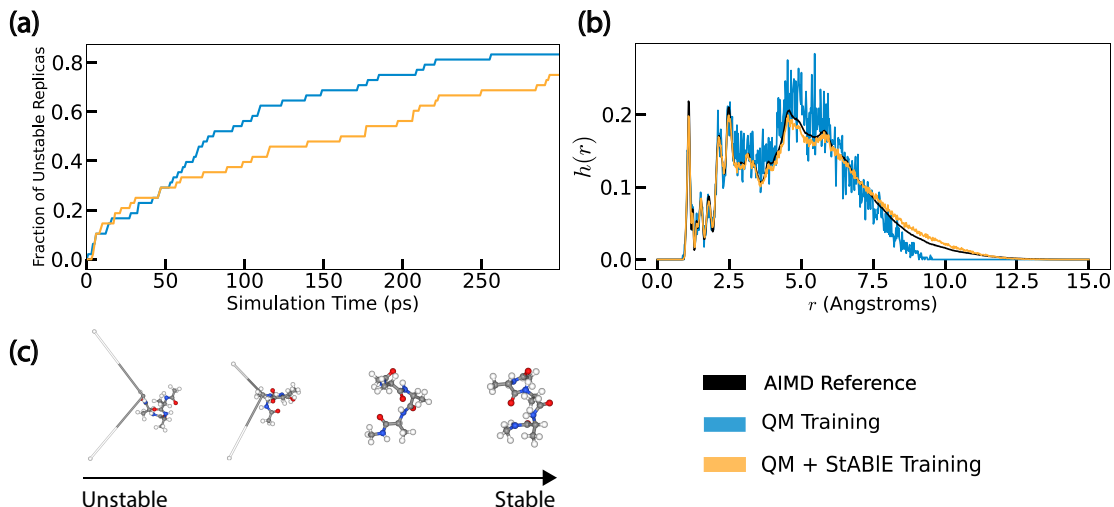


Figure 5: Ac-Ala3-NHMe tetrapeptide simulation with StABIE Training. Results of StABIE Training a NequIP [5] NNIP on the 42-atom Ac-Ala3-NHMe tetrapeptide from the MD22 [17] dataset at 500 Kelvin. **(a)** Fraction of unstable replicas as a function of simulation time for a NequIP NNIP trained on 1,000 energy and forces reference data points (blue). Applying StABIE Training yields a model which can simulate more MD replicas stably over time (orange). **(b)** Distribution of interatomic distances ($h(r)$) from an *ab-initio* molecular dynamics (AIMD) simulation (black), a NequIP model trained on 14,890 QM data points (blue), and a NequIP model trained on 14,890 QM datapoints, followed by our StABIE Training procedure (orange). The StABIE-trained NequIP model much more closely recovers the true $h(r)$, while the $h(r)$ produced by the model trained only on QM reference data is noisy and inaccurate due to insufficient sampling time. **(c)** Ac-Ala3-NHMe structures sampled over epochs of a single learning phase of StABIE Training. There is a clear progression as very unstable configurations become stable.

version of the Boltzmann gradient estimator (Equation 8) in order to guide the optimization process towards specific spatial domains of instability.

Problem setup. We pre-train a GemNet-T model to the energy and forces matching objective using a subset of 1,000 reference structures from the training dataset. After convergence, we begin StABIE Training with the localized Boltzmann estimator, simulating 10 parallel replicas at a temperature of 300K. We use a minimum intermolecular distance criterion (see Supplementary Section A.5) to detect instabilities. To estimate gradients for optimization, from each global state we extract all possible local neighborhoods containing a single water molecule (see Supplementary Section A.6 for more details on the local neighborhood sampling scheme). The most prevalent failure mode in this system is unphysical bond stretching, which eventually leads to collisions with nearby water molecules. Motivated by this observation, we use the mean hydrogen-oxygen bond length as our training observable. We perform a single cycle of simulation and learning.

Results. We evaluate the performance of the StABIE-Trained model by performing 10 parallel MD simulations at 300K, starting from held-out initial conditions. We achieve significant improvements in stability and accuracy using our training approach. We nearly double the stable simulation time relative to a baseline NNIP model trained only on QM reference data (Figure 6b). Compared to a reference value of $2.3 \times 10^{-9} \frac{m^2}{s}$, the mean diffusivity produced by StABIE-trained model simulations is $1.6 \times 10^{-9} \frac{m^2}{s}$, while the mean diffusivity produced by baseline model simulations is $5.0 \times 10^{-9} \frac{m^2}{s}$ (Figure 6c). This corresponds to an 87% improvement in the accuracy of diffusivity coefficient estimation. We note that the StABIE-trained model

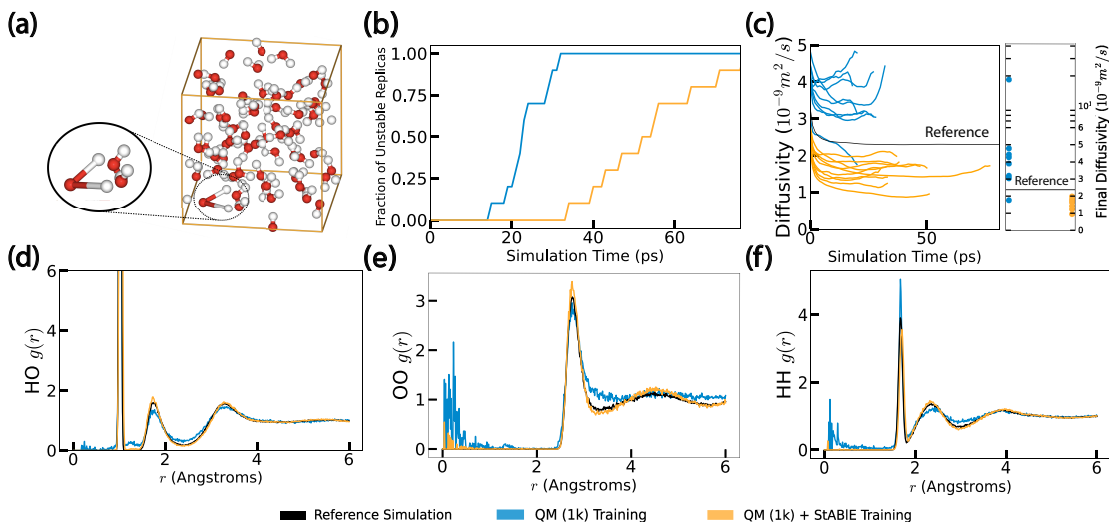


Figure 6: All-Atom Water Simulation with StABIE Training. Results of StABIE Training a GemNet-T [24] NNIP on an all-atom water system with 64 molecules at 300 Kelvin. **(a)** Example unstable configuration arising in a GemNet-T simulation of water. Instabilities are highly localized and manifest as unphysical bond stretches or intermolecular collisions, motivating the use of our localized Boltzmann estimator (Section 22.1) during training **(b)** Fraction of unstable replicas as a function of simulation time for a GemNet-T NNIP trained on energy and forces reference data points (blue), followed by StABIE Training (orange). StABIE Training yields a clear stability improvement relative to training on only energy and forces data, more than doubling the median stable simulation time from 23 to 52 picoseconds. **(c)** Left: Convergence of the diffusivity coefficient over the simulations produced by the reference Extended Simple Point Charge model [73] (black), a GemNet-T model trained on 1,000 energy and forces datapoints (blue), and a GemNet-T model trained on 1,000 energy and forces datapoints followed by StABIE Training (orange). Right: Relative to the reference value of $2.3 \times 10^{-9} \frac{m^2}{s}$ The StABIE-trained model gives a more accurate final estimate of the diffusivity coefficient, with a mean predicted value of $1.6 \times 10^{-9} \frac{m^2}{s}$ as compared with a value of $5.0 \times 10^{-9} \frac{m^2}{s}$ produced by the baseline model. **(d - f)** Element-conditioned (OH, OO, HH) radial distribution functions (RDF) produced by simulations from the reference model (black), a GemNet-T model trained on 1,000 energy and forces data points (blue), and a GemNet-T model trained on 1,000 energy and forces data points followed by StABIE Training (orange). The StABIE-trained model produces fewer unphysical collisions and more accurately captures long-range interactions.

systemically underestimates the reference diffusivity, while the baseline model overestimates the value. We hypothesize that in this particular case, StABIE Training has a retarding effect on system dynamics. As the StABIE optimization process assigns high probability to microstates closely matching the equilibrium bond length, small fluctuations about this value may be excessively penalized, inhibiting the motion of molecules in the simulation. Finally, the spikes in the short-range region of the element-conditioned RDFs (Figures 6d-f), which indicate unphysical bond stretching and collision events, are largely removed in StABIE-trained model simulations, while long-range correlations are also better captured. We reiterate that in this experiment, neither the element-conditioned RDFs nor the diffusivity coefficient were explicitly seen during StABIE Training.

4 Discussion

We have introduced StABIE Training, a strategy for training stable and accurate neural network interatomic potentials. We have demonstrated StABIE Training on a flexible organic molecule, a tetrapeptide, and a liquid-phase system, as well as with three modern NNIP architectures. Our training procedure results in NNIPs which remain stable for considerably longer periods in MD simulation compared to models trained

only on QM data, and as a result, more accurately reproduce key simulation observables. We also note that we have improved the recovery of observables that the NNIPs were not explicitly trained on. These include dynamical observables such as the diffusivity coefficient of water and velocity autocorrelation function of aspirin. We showed that StABIE-trained models exhibit better generalization to unseen temperatures for the aspirin molecule. Finally, we demonstrated that StABIE-trained models can outperform NNIP models trained on up to 50 times more QM data. We thus expect StABIE Training to be a particularly compelling alternative to traditional QM training in cases where producing comprehensive *ab-initio* datasets is prohibitively expensive, such as for large system sizes.

Advantages of StABIE Training. One advantage of StABIE Training is that it can utilize both quantum-mechanical energies and forces and system observables to supervise NNIP training. As reference observables can be easily computed by averaging over existing datasets, the stability, accuracy, and data efficiency gains brought by StABIE Training require *no additional reference calculations or data*. StABIE Training is thus self-contained and efficient, requiring minimal additional computational expense beyond conventional NNIP training (see Supplementary Section A.6 for details on training times).

StABIE Training can also be flexibly applied across atomistic systems due to its ability to handle a diverse set of failure modes arising in MD simulation, including both global and local instabilities. Specifically, due to our localized Boltzmann estimator, we can target and resolve isolated instabilities found in simulations of large condensed-phase systems. The adaptability of our method is further exemplified by the lack of reliance on a manually specified prior potential, a common requirement of observable-based learning schemes. The pre-training step which precedes StABIE Training effectively learns a QM-informed prior, which is then further refined in the alternating simulation and learning stages.

The flexibility of StABIE Training extends to the neural network parameterization of the potential energy function. The three NNIP architectures we considered in this work vary widely in their expressivity, as measured by the number of total learnable parameters, as well as in the symmetry principles governing their internal feature transformations (see Supplementary Section A.6 for details). The effectiveness of StABIE Training across these models suggests that our approach will remain applicable as NNIP architectures continue to evolve.

Finally, we note that the underlying Boltzmann gradient estimator used to train the NNIPs differentiates through the potential energy of uncorrelated states. It is thus agnostic to the method of sampling from the Boltzmann distribution $P_\theta(\Gamma)$, and is readily applicable to sampling schemes other than MD simulation (e.g., Monte Carlo methods). This is related to recent work in machine learning on implicit layers, which enables differentiation of optimization problem solutions without knowledge of the numerical solver used [1, 28, 53, 9, 49].

Limitations. A limitation of StABIE Training is that training NNIPs to match reference observables lacks the convergence guarantees provided by traditional QM learning in the large data limit. Specifically, the observable-matching objective is under-constrained, as the mapping between a potential energy function and a sparse set of simulation observables is in general non-unique [50]. Although we mitigate this problem by pre-training and regularizing StABIE Training with the conventional energy and forces loss function, we observe that stability improvements resulting from StABIE Training are accompanied by a minor increase in the energy and forces error on a held-out test set, indicating a misalignment between the observable-matching and QM objectives. Adjusting the strength of the QM regularization and the learning rate used for StABIE Training are two primary ways in which to navigate this tradeoff. We note, however, that our

observed error increases are typically within the range of DFT error (see Supplementary Section A.10 for details). We also note that StABIE Training is currently incompatible with dynamical observables, due to the use of uncorrelated states to compute the Boltzmann Estimator. Overcoming this limitation is non-trivial, as it requires optimization over long paths, which is a significantly higher-dimensional problem with large-variance gradients [10].

Future Work. In this work, we took observables calculated from high-fidelity simulations as reference values. Many of the observables we considered, such as the radial distribution function, diffusivity coefficient, and equilibrium bond length, are also experimentally measurable. Future work could explore training with experimental observables from multiple thermodynamic conditions (e.g., temperatures and pressures) simultaneously to yield more generalizable and robust potentials. As an independent source of information, experimental observables could also be used to refine NNIPs trained on data obtained from lower levels of theory. Future work could also explore incorporating additional observables into StABIE Training, particularly those which are dynamical. This could restrict the set of learnable functions and address the under-constrained nature of learning with observables. Finally, we note that established techniques, such as active learning [62, 68, 41], are not mutually exclusive with StABIE Training, and could be used in tandem to further improve NNIP stability and robustness.

5 Acknowledgements

This work was initially supported by Laboratory Directed Research and Development (LDRD) funding under Contract Number DE-AC02-05CH11231. It was then supported by the U.S. Department of Energy, Office of Science, Office of Advanced Scientific Computing Research, Scientific Discovery through Advanced Computing (SciDAC) program under contract No. DE-AC02-05CH11231. This research used resources of the National Energy Research Scientific Computing Center (NERSC), a U.S. Department of Energy Office of Science User Facility located at Lawrence Berkeley National Laboratory, operated under Contract No. DE-AC02-05CH11231. We thank Rasmus Lindrup, Toby Kreiman, Geoffrey Negiar, Muhammad Hasyim, Ritwik Gupta, Aayush Singh, David Limmer, Kranthi Mandadapu, David Prendergast, Bryan McCloskey, and Muratahan Aykol for fruitful discussions and comments on the manuscript.

6 Author Contributions

S.R and A.S.K. jointly conceived and initiated the project. S.R. conceptualized and implemented the Localized Boltzmann Estimator and StABIE Training method, and performed experiments. I.A. trained the baseline models and contributed to the Boltzmann Estimator theory. F.P contributed to a unique derivation and analysis of the Boltzmann Estimator. A.S.K. supervised and guided the project from conception to design of experiments, implementation, theory, and analysis. All authors analyzed results and wrote the paper.

7 Code Availability

Our code will be made available at <https://github.com/ASK-Berkeley/StABIE-Training>.

References

- [1] Brandon Amos and J. Zico Kolter. “OptNet: Differentiable optimization as a layer in neural networks”. In: *Proceedings of the International Conference on Machine Learning (ICML)*. 2017, pp. 136–145.
- [2] A. P. Bartók et al. “Gaussian approximation potentials: The accuracy of quantum mechanics, without the electrons”. In: *Phys. Rev. Lett.* 104 (2010), p. 136403.
- [3] Ilyes Batatia et al. *A foundation model for atomistic materials chemistry*. 2023. arXiv: 2401.00096 [physics.chem-ph].
- [4] Ilyes Batatia et al. “MACE: Higher Order Equivariant Message Passing Neural Networks for Fast and Accurate Force Fields”. In: *Neural Information Processing Systems (NeurIPS)*. 2022.
- [5] Simon Batzner et al. “E(3)-equivariant graph neural networks for data-efficient and accurate interatomic potentials”. In: *Nature Communications* 13.1 (May 2022). DOI: 10.1038/s41467-022-29939-5.
- [6] J. Behler. “Neural network potential-energy surfaces in chemistry: A tool for large-scale simulations”. In: *Phys. Chem. Chem. Phys.* 13 (2011), pp. 17930–17955.
- [7] Jörg Behler and Michele Parrinello. “Generalized Neural-Network Representation of High-Dimensional Potential-Energy Surfaces”. In: *Phys. Rev. Lett.* 98 (14 Apr. 2007), p. 146401. DOI: 10.1103/PhysRevLett.98.146401. URL: <https://link.aps.org/doi/10.1103/PhysRevLett.98.146401>.
- [8] Vaibhav Bihani et al. *EGraFFBench: Evaluation of Equivariant Graph Neural Network Force Fields for Atomistic Simulations*. 2023. arXiv: 2310.02428 [cs.LG].
- [9] Mathieu Blondel et al. “Efficient and Modular Implicit Differentiation”. In: *Neural Information Processing Systems (NeurIPS)*. Google Research. 2022.
- [10] Peter G. Bolhuis, Z. Faidon Brotzakis, and Bettina G. Keller. “Optimizing molecular potential models by imposing kinetic constraints with path reweighting”. In: *J. Chem. Phys.* 159 (2023), p. 074102. DOI: 10.1063/5.0151166. URL: <https://doi.org/10.1063/5.0151166>.
- [11] Max Born and J. Robert Oppenheimer. “On the Quantum Theory of Molecules”. In: *Annalen der Physik* 389.20 (1927). In German, pp. 457–484. DOI: 10.1002/andp.19273892002.
- [12] R. Car and M. Parrinello. “Unified Approach for Molecular Dynamics and Density-Functional Theory”. In: *Phys. Rev. Lett.* 55 (1985). Published 25 November 1985, p. 2471. DOI: 10.1103/PhysRevLett.55.2471.
- [13] Scott P. Carmichael and M. Scott Shell. “A New Multiscale Algorithm and Its Application to Coarse-Grained Peptide Models for Self-Assembly”. In: *J. Phys. Chem. B* 116.29 (2012), pp. 8383–8393. DOI: 10.1021/jp2114994.
- [14] Nicholas E. Charron et al. *Navigating protein landscapes with a machine-learned transferable coarse-grained model*. 2023. arXiv: 2310.18278 [q-bio.BM].
- [15] C. Chen and S.P. Ong. “A universal graph deep learning interatomic potential for the periodic table”. In: *Nat Comput Sci* 2 (2022), pp. 718–728. DOI: 10.1038/s43588-022-00349-3. URL: <https://doi.org/10.1038/s43588-022-00349-3>.

- [16] Bingqing Cheng et al. “Ab initio thermodynamics of liquid and solid water”. In: *Proc. Natl. Acad. Sci. U.S.A.* 116.4 (Jan. 2019). Edited by Pablo G. Debenedetti, Princeton University, Princeton, NJ, approved December 3, 2018 (received for review September 4, 2018), pp. 1110–1115. DOI: [10.1073/pnas.1815117116](https://doi.org/10.1073/pnas.1815117116). URL: <https://doi.org/10.1073/pnas.1815117116>.
- [17] Stefan Chmiela et al. *Accurate global machine learning force fields for molecules with hundreds of atoms*. 2022. arXiv: [2209.14865](https://arxiv.org/abs/2209.14865) [physics.chem-ph].
- [18] Stefan Chmiela et al. “Machine learning of accurate energy-conserving molecular force fields”. In: *Science Advances* 3.5 (May 2017). DOI: [10.1126/sciadv.1603015](https://doi.org/10.1126/sciadv.1603015).
- [19] Bowen Deng et al. “CHGNet as a pretrained universal neural network potential for charge-informed atomistic modelling”. In: *Nature Machine Intelligence* 5.9 (2023), pp. 1031–1041.
- [20] FA Faber et al. “Prediction Errors of Molecular Machine Learning Models Lower than Hybrid DFT Error”. In: *J Chem Theory Comput* 13.11 (Nov. 2017). Epub 2017 Oct 10, pp. 5255–5264. DOI: [10.1021/acs.jctc.7b00577](https://doi.org/10.1021/acs.jctc.7b00577).
- [21] Daan Frenkel and Berend Smit. *Understanding Molecular Simulation: From Algorithms to Applications*. 2nd ed. Academic Press, Nov. 2001.
- [22] Richard A. Friesner. “Ab initio quantum chemistry: Methodology and applications”. In: *Proceedings of the National Academy of Sciences* 102.19 (May 2005), pp. 6648–6653. DOI: [10.1073/pnas.0408036102](https://doi.org/10.1073/pnas.0408036102).
- [23] Xiang Fu et al. *Forces are not Enough: Benchmark and Critical Evaluation for Machine Learning Force Fields with Molecular Simulations*. 2022. arXiv: [2210.07237](https://arxiv.org/abs/2210.07237) [physics.comp-ph].
- [24] Johannes Gasteiger, Florian Becker, and Stephan Günnemann. In: *Conference on Neural Information Processing Systems (NeurIPS)*. 2021.
- [25] Johannes Gasteiger, Janek Groß, and Stephan Günnemann. “Directional message passing for molecular graphs”. In: *8th International Conference on Learning Representations, ICLR*. 2020.
- [26] Johannes Gasteiger et al. *GemNet-OC: Developing Graph Neural Networks for Large and Diverse Molecular Simulation Datasets*. 2022. arXiv: [2204.02782](https://arxiv.org/abs/2204.02782) [cs.LG].
- [27] Mario Geiger and Tess Smidt. *e3nn: Euclidean Neural Networks*. 2022. arXiv: [2207.09453](https://arxiv.org/abs/2207.09453) [cs.LG].
- [28] S. Gould et al. “On differentiating parameterized argmin and argmax problems with application to bi-level optimization”. In: *arXiv preprint arXiv:1607.05447* (2016).
- [29] Weihua Hu et al. *ForceNet: A Graph Neural Network for Large-Scale Quantum Calculations*. 2021. arXiv: [2103.01436](https://arxiv.org/abs/2103.01436) [cs.LG].
- [30] John Ingraham et al. “Learning Protein Structure with a Differentiable Simulator”. In: *International Conference on Learning Representations, ICLR*. 2019.
- [31] R. O. Jones. “Density functional theory: Its origins, rise to prominence, and future”. In: *Rev. Mod. Phys.* 87 (3 Aug. 2015), pp. 897–923. DOI: [10.1103/RevModPhys.87.897](https://doi.org/10.1103/RevModPhys.87.897). URL: <https://link.aps.org/doi/10.1103/RevModPhys.87.897>.
- [32] A. Kabylda et al. “Efficient interatomic descriptors for accurate machine learning force fields of extended molecules”. In: *Nat Commun* 14.1 (June 2023). Erratum in: *Nat Commun*. 2023 Jul 11;14(1):4116. PMID: 37322039; PMCID: PMC10272221., p. 3562. DOI: [10.1038/s41467-023-39214-w](https://doi.org/10.1038/s41467-023-39214-w).
- [33] Thomas N. Kipf and Max Welling. *Semi-Supervised Classification with Graph Convolutional Networks*. 2017. arXiv: [1609.02907](https://arxiv.org/abs/1609.02907) [cs.LG].

- [34] Christopher Kolloff and Simon Olsson. “Rescuing off-equilibrium simulation data through dynamic experimental data with dynAMMo”. In: *Mach. Learn.: Sci. Technol.* 4.4 (2023). © 2023 The Author(s), p. 045050. DOI: [10.1088/2632-2153/ac7b4f](https://doi.org/10.1088/2632-2153/ac7b4f).
- [35] Dávid Péter Kovács et al. “Linear Atomic Cluster Expansion Force Fields for Organic Molecules: Beyond RMSE”. In: *Journal of Chemical Theory and Computation* 17.12 (2021). PMID: 34735161, pp. 7696–7711. DOI: [10.1021/acs.jctc.1c00647](https://doi.org/10.1021/acs.jctc.1c00647). eprint: <https://doi.org/10.1021/acs.jctc.1c00647>. URL: <https://doi.org/10.1021/acs.jctc.1c00647>.
- [36] Dávid Péter Kovács et al. *MACE-OFF23: Transferable Machine Learning Force Fields for Organic Molecules*. 2023. arXiv: 2312.15211 [physics.chem-ph].
- [37] Boris Kozinsky et al. “Scaling the Leading Accuracy of Deep Equivariant Models to Biomolecular Simulations of Realistic Size”. In: *Proceedings of the International Conference for High Performance Computing, Networking, Storage and Analysis*. SC ’23. Denver, CO, USA: Association for Computing Machinery, 2023. ISBN: 9798400701092. DOI: [10.1145/3581784.3627041](https://doi.org/10.1145/3581784.3627041). URL: <https://doi.org/10.1145/3581784.3627041>.
- [38] Aditi S Krishnapriyan et al. “Learning continuous models for continuous physics”. In: *Communications Physics* 6.1 (2023), p. 319.
- [39] H. G. Kümmer. “A biography of the coupled cluster method”. In: *Recent Progress in Many-Body Theories*. Ed. by R. F. Bishop et al. Singapore: World Scientific Publishing, 2002, pp. 334–348.
- [40] Ask Hjorth Larsen et al. “The atomic simulation environment — a python library for working with atoms”. In: *Journal of Physics: Condensed Matter* (2017). DOI: [10.1088/1361-648X/aa680e](https://doi.org/10.1088/1361-648X/aa680e).
- [41] Qidong Lin et al. “Searching Configurations in Uncertainty Space: Active Learning of High-Dimensional Neural Network Reactive Potentials”. In: *J. Chem. Theory Comput.* 17.5 (2021), pp. 2691–2701. DOI: [10.1021/acs.jctc.0c01193](https://doi.org/10.1021/acs.jctc.0c01193).
- [42] Yi Liu et al. “Spherical Message Passing for 3D Molecular Graphs”. In: *International Conference on Learning Representations (ICLR)*. 2022.
- [43] M. Majewski, A. Pérez, P. Thölke, et al. “Machine learning coarse-grained potentials of protein thermodynamics”. In: *Nat Commun* 14 (2023), p. 5739. DOI: [10.1038/s41467-023-41343-1](https://doi.org/10.1038/s41467-023-41343-1). URL: <https://doi.org/10.1038/s41467-023-41343-1>.
- [44] TE Markland and M Ceriotti. “Nuclear quantum effects enter the mainstream”. In: *Nat Rev Chem* 2 (2018), p. 0109. DOI: [10.1038/s41570-017-0109](https://doi.org/10.1038/s41570-017-0109).
- [45] A. Merchant, S. Batzner, S.S. Schoenholz, et al. “Scaling deep learning for materials discovery”. In: *Nature* 624 (2023), pp. 80–85. DOI: [10.1038/s41586-023-06735-9](https://doi.org/10.1038/s41586-023-06735-9).
- [46] Joe D. Morrow, John L. A. Gardner, and Volker L. Deringer. “How to validate machine-learned interatomic potentials”. In: *J. Chem. Phys.* 158 (2023), p. 121501.
- [47] Albert Musaelian et al. *Learning Local Equivariant Representations for Large-Scale Atomistic Dynamics*. 2022. arXiv: 2204.05249 [physics.comp-ph].
- [48] Carles Navarro, Maciej Majewski, and Gianni De Fabritiis. “Top-Down Machine Learning of Coarse-Grained Protein Force Fields”. In: *J. Chem. Theory Comput.* (2023).
- [49] Geoffrey Négiar, Michael W. Mahoney, and Aditi Krishnapriyan. “Learning differentiable solvers for systems with hard constraints”. In: *The Eleventh International Conference on Learning Representations*. 2023.

- [50] W. G. Noid. “Perspective: coarse-grained models for biomolecular systems”. In: *J. Chem. Phys.* 139 (2013), p. 090901.
- [51] John P. Perdew, Kieron Burke, and Matthias Ernzerhof. “Generalized Gradient Approximation Made Simple”. In: *Phys. Rev. Lett.* 77 (18 Oct. 1996), pp. 3865–3868. DOI: [10.1103/PhysRevLett.77.3865](https://doi.org/10.1103/PhysRevLett.77.3865). URL: <https://link.aps.org/doi/10.1103/PhysRevLett.77.3865>.
- [52] Z Raza et al. “Proton ordering in cubic ice and hexagonal ice; a potential new ice phase–XIc”. In: *Phys. Chem. Chem. Phys.* 13 (2011), pp. 19788–19795. DOI: [10.1039/c1cp22167a](https://doi.org/10.1039/c1cp22167a).
- [53] Jie Ren et al. *TorchOpt: An Efficient Library for Differentiable Optimization*. 2022. arXiv: [2211.06934](https://arxiv.org/abs/2211.06934) [cs.MS].
- [54] Sebastien Röcken and Julija Zavadlav. *Accurate machine learning force fields via experimental and simulation data fusion*. 2023. arXiv: [2308.09142](https://arxiv.org/abs/2308.09142) [physics.chem-ph].
- [55] M. Rupp et al. “Fast and accurate modeling of molecular atomization energies with machine learning”. In: *Phys. Rev. Lett.* 108 (2012), p. 058301.
- [56] Franco Scarselli et al. “The Graph Neural Network Model”. In: *IEEE Transactions on Neural Networks* 20.1 (2009), pp. 61–80. DOI: [10.1109/TNN.2008.2005605](https://doi.org/10.1109/TNN.2008.2005605).
- [57] Michael Schaarschmidt et al. *Learned Force Fields Are Ready For Ground State Catalyst Discovery*. 2022. arXiv: [2209.12466](https://arxiv.org/abs/2209.12466) [cond-mat.mtrl-sci].
- [58] K. T. Schütt et al. “SchNet – A deep learning architecture for molecules and materials”. In: *J. Chem. Phys.* 148.24 (June 2018), p. 241722. DOI: [10.1063/1.5019779](https://doi.org/10.1063/1.5019779). URL: <https://doi.org/10.1063/1.5019779>.
- [59] Kristof T. Schütt, Oliver T. Unke, and Michael Gastegger. “Equivariant message passing for the prediction of tensorial properties and molecular spectra”. In: *International Conference on Machine Learning (ICML)*. 2021.
- [60] Nima Shoghi et al. *From Molecules to Materials: Pre-training Large Generalizable Models for Atomic Property Prediction*. 2023. arXiv: [2310.16802](https://arxiv.org/abs/2310.16802) [cs.LG].
- [61] Martin Šípka et al. *Differentiable Simulations for Enhanced Sampling of Rare Events*. 2023. arXiv: [2301.03480](https://arxiv.org/abs/2301.03480) [physics.chem-ph].
- [62] Justin S. Smith et al. “Less is more: Sampling chemical space with active learning”. In: *J. Chem. Phys.* 148 (2018), p. 241733. DOI: [10.1063/1.5023802](https://doi.org/10.1063/1.5023802).
- [63] Sina Stocker et al. “How robust are modern graph neural network potentials in long and hot molecular dynamics simulations?” In: *Machine Learning: Science and Technology* 3.4 (Nov. 2022), p. 045010. DOI: [10.1088/2632-2153/ac9955](https://doi.org/10.1088/2632-2153/ac9955). URL: <https://dx.doi.org/10.1088/2632-2153/ac9955>.
- [64] S. Takamoto, C. Shinagawa, D. Motoki, et al. “Towards universal neural network potential for material discovery applicable to arbitrary combination of 45 elements”. In: *Nat Commun* 13 (2022), p. 2991. DOI: [10.1038/s41467-022-30687-9](https://doi.org/10.1038/s41467-022-30687-9). URL: <https://doi.org/10.1038/s41467-022-30687-9>.
- [65] Sebastian Thaler and Julija Zavadlav. “Learning neural network potentials from experimental data via Differentiable Trajectory Reweighting”. In: *Nature Communications* 12 (2021), p. 6884. DOI: [10.1038/s41467-021-27241-4](https://doi.org/10.1038/s41467-021-27241-4).

- [66] Alexandre Tkatchenko and Matthias Scheffler. “Accurate Molecular Van Der Waals Interactions from Ground-State Electron Density and Free-Atom Reference Data”. In: *Phys. Rev. Lett.* 102 (7 Feb. 2009), p. 073005. DOI: [10.1103/PhysRevLett.102.073005](https://doi.org/10.1103/PhysRevLett.102.073005). URL: <https://link.aps.org/doi/10.1103/PhysRevLett.102.073005>.
- [67] Alexandre Tkatchenko et al. “Accurate and Efficient Method for Many-Body van der Waals Interactions”. In: *Phys. Rev. Lett.* 108 (23 June 2012), p. 236402. DOI: [10.1103/PhysRevLett.108.236402](https://doi.org/10.1103/PhysRevLett.108.236402). URL: <https://link.aps.org/doi/10.1103/PhysRevLett.108.236402>.
- [68] J. Vandermause, S.B. Torrisi, S. Batzner, et al. “On-the-fly active learning of interpretable Bayesian force fields for atomistic rare events”. In: *npj Comput Mater* 6 (2020), p. 20. DOI: [10.1038/s41524-020-0283-z](https://doi.org/10.1038/s41524-020-0283-z). URL: <https://doi.org/10.1038/s41524-020-0283-z>.
- [69] Joshua A. Vita and Daniel Schwalbe-Koda. “Data efficiency and extrapolation trends in neural network interatomic potentials”. In: *Mach. Learn.: Sci. Technol.* 4 (2023), p. 035031.
- [70] Wujie Wang, Simon Axelrod, and Rafael Gómez-Bombarelli. *Differentiable Molecular Simulations for Control and Learning*. 2020. arXiv: 2003.00868 [physics.comp-ph].
- [71] Wujie Wang et al. “Learning pair potentials using differentiable simulations”. In: *The Journal of Chemical Physics* 158.4 (Jan. 2023), p. 044113. DOI: [10.1063/5.0126475](https://doi.org/10.1063/5.0126475).
- [72] Zun Wang et al. “Improving machine learning force fields for molecular dynamics simulations with fine-grained force metrics”. In: *J. Chem. Phys.* 159 (2023), p. 035101. DOI: [10.1063/5.0147023](https://doi.org/10.1063/5.0147023).
- [73] Yujie Wu, Harald L. Tepper, and Gregory A. Voth. “Flexible simple point-charge water model with improved liquid-state properties”. In: *The Journal of Chemical Physics* 124.2 (Jan. 2006), p. 024503. ISSN: 0021-9606, 1089-7690. DOI: [10.1063/1.2136877](https://doi.org/10.1063/1.2136877).
- [74] Robert W. Zwanzig. “High-Temperature Equation of State by a Perturbation Method. I. Nonpolar Gases”. In: *J. Chem. Phys.* 22 (1954), pp. 1420–1426.

A Supplementary Information

A.1 Derivation of Boltzmann Estimator

We provide a full derivation of our Boltzmann estimator, which we use to train our NNIP as part of StABIE Training. Consider a vector-valued observable $g(\Gamma)$ of a state Γ , and a reference value of the observable g_{ref} . Training a NNIP U_θ to match g_{ref} requires minimizing the loss function,

$$\mathcal{L}_{\text{obs}}(\theta) \stackrel{\text{def}}{=} \|\mathbb{E}_{\Gamma \sim P_\theta(\Gamma)}[g(\Gamma)] - g_{\text{ref}}\|_2^2,$$

where $P_\theta(\Gamma)$ is the equilibrium distribution induced by the NNIP U_θ . This requires computing the gradient, $\nabla_\theta \mathcal{L}_{\text{obs}}$, which can be decomposed via the chain rule as follows:

$$\begin{aligned} \nabla_\theta \mathcal{L}_{\text{obs}}^\top &= \frac{\partial \mathcal{L}_{\text{obs}}}{\partial \mathbb{E}_{\Gamma \sim P_\theta(\Gamma)}[g(\Gamma)]} \frac{\partial \mathbb{E}_{\Gamma \sim P_\theta(\Gamma)}[g(\Gamma)]}{\partial \theta} \\ &= 2(\mathbb{E}_{\Gamma \sim P_\theta(\Gamma)}[g(\Gamma)] - g_{\text{ref}})^\top \frac{\partial \mathbb{E}_{\Gamma \sim P_\theta(\Gamma)}[g(\Gamma)]}{\partial \theta}. \end{aligned}$$

We derive the N -sample estimator, presented in Equation 6, of the Jacobian, $\partial \mathbb{E}_{\Gamma \sim P_\theta(\Gamma)}[g(\Gamma)]/\partial \theta$. The estimator is repeated below for convenience.

$$\mathcal{E}(\Gamma^{(1)}, \dots, \Gamma^{(N)}) \stackrel{\text{def}}{=} \frac{N}{k_B T(N-1)} \left[\hat{\mathbb{E}}[g(\Gamma)] \hat{\mathbb{E}}[\nabla_\theta U_\theta(\Gamma)]^\top - \hat{\mathbb{E}}[g(\Gamma) \nabla_\theta U_\theta(\Gamma)^\top] \right],$$

where $\hat{\mathbb{E}}$ denotes sample averages. This is an unbiased estimator, that is, $\mathbb{E}_{(\Gamma^{(1)}, \dots, \Gamma^{(N)}) \sim P_\theta(\Gamma)}[\mathcal{E}(\Gamma^{(1)}, \dots, \Gamma^{(N)})] = \frac{\partial \mathbb{E}_{\Gamma \sim P_\theta(\Gamma)}[g(\Gamma)]}{\partial \theta}$.

Proof. Given $P_\theta(\Gamma) \stackrel{\text{def}}{=} \frac{\exp\left(-\frac{1}{k_B T} \mathcal{H}_\theta(\Gamma)\right)}{C(\theta)}$, where $\mathcal{H}(\Gamma) = \sum_{i=1}^N \frac{p_i^2}{2m_i} + U_\theta(r)$, and $C(\theta) \stackrel{\text{def}}{=} \int \exp\left(-\frac{1}{k_B T} \mathcal{H}_\theta(\Gamma')\right) d\Gamma'$ is the partition function, we have,

$$\begin{aligned} \frac{\partial \mathbb{E}_{\Gamma \sim P_\theta(\Gamma)}[g(\Gamma)]}{\partial \theta} &= \frac{\partial}{\partial \theta} \int g(\Gamma') P_\theta(\Gamma') d\Gamma' \\ &= \int g(\Gamma') \nabla_\theta P_\theta(\Gamma')^\top d\Gamma' \\ &= \int g(\Gamma') \nabla_\theta \left(\frac{\exp\left(-\frac{1}{k_B T} \mathcal{H}_\theta(\Gamma)\right)}{C(\theta)} \right)^\top d\Gamma'. \end{aligned}$$

Expanding via the chain rule for Jacobians, and noting that $\nabla_\theta \mathcal{H}_\theta(\Gamma) = \nabla_\theta U_\theta(r)$ (we will write $U_\theta(\Gamma)$ for convenience), we get,

$$\begin{aligned} &= \int g(\Gamma') \frac{-\frac{1}{k_B T} \exp\left(-\frac{1}{k_B T} \mathcal{H}_\theta(\Gamma')\right) \nabla_\theta U_\theta(\Gamma')^\top C(\theta) - \nabla_\theta C(\theta)^\top \exp\left(-\frac{1}{k_B T} \mathcal{H}_\theta(\Gamma')\right)}{C(\theta)^2} d\Gamma' \\ &= \int g(\Gamma') \left[-\frac{1}{k_B T} \nabla_\theta U_\theta(\Gamma')^\top P_\theta(\Gamma') - \frac{\nabla_\theta C(\theta)^\top}{C(\theta)} P_\theta(\Gamma') \right] d\Gamma'. \end{aligned}$$

By definition of $C(\theta)$, the quotient $\frac{\nabla_\theta C(\theta)}{C(\theta)}$ can be simplified as,

$$\begin{aligned}\frac{\nabla_\theta C(\theta)}{C(\theta)} &= \frac{-\int \nabla_\theta U_\theta(\Gamma') \exp\left(-\frac{1}{k_B T} \mathcal{H}_\theta(\Gamma')\right) d\Gamma'}{k_B T \cdot C(\theta)} \\ &= -\frac{1}{k_B T} \int \nabla_\theta U_\theta(\Gamma') P_\theta(\Gamma') d\Gamma' \\ &= -\frac{1}{k_B T} \mathbb{E}_\Gamma[\nabla_\theta U_\theta(\Gamma)].\end{aligned}$$

Putting it all together, we have,

$$\begin{aligned}\frac{\partial \mathbb{E}_{\Gamma \sim P_\theta(\Gamma)}[g(\Gamma)]}{\partial \theta} &= -\frac{1}{k_B T} \left(\underbrace{\int g(\Gamma') \nabla_\theta U_\theta(\Gamma')^\top P_\theta(\Gamma') d\Gamma'}_{\mathbb{E}[g(\Gamma) \cdot \nabla_\theta U_\theta(\Gamma)]} - \underbrace{\left(\int g(\Gamma') \cdot P_\theta(\Gamma') \cdot d\Gamma' \right)}_{\mathbb{E}[g(\Gamma)]} \mathbb{E}[\nabla_\theta U_\theta(\Gamma)]^\top \right) \\ &= -\frac{1}{k_B T} \left(\mathbb{E} \left[g(\Gamma) \cdot \nabla_\theta U_\theta(\Gamma)^\top \right] - \mathbb{E}[g(\Gamma)] \mathbb{E}[\nabla_\theta U_\theta(\Gamma)]^\top \right) \\ &= -\frac{1}{k_B T} \text{Cov}(g(\Gamma), \nabla_\theta U_\theta(\Gamma)).\end{aligned}$$

In this work, we use the following unbiased estimator for covariance. Given 2 random vectors X, Y , and samples of these vectors $\{(X^{(1)}, Y^{(1)}), \dots, (X^{(N)}, Y^{(N)})\}$, our estimator is given by:

$$\widehat{\text{Cov}}(X, Y) = \frac{1}{N-1} \sum_{i=1}^N X^{(i)} Y^{(i)\top} - \frac{1}{N(N-1)} \left(\sum_{j=1}^N X^{(j)} \right) \left(\sum_{k=1}^N Y^{(k)\top} \right).$$

We can prove it is unbiased by taking the expectation of the right hand side and applying linearity of expectation:

$$\begin{aligned}&= \frac{1}{N-1} \sum_{i=1}^N \mathbb{E}[X^{(i)} Y^{(i)\top}] - \frac{1}{N(N-1)} \left(\sum_{i=1}^N \mathbb{E}[X^{(i)} Y^{(i)\top}] + \sum_{j \neq k} \mathbb{E}[X^{(j)} Y^{(k)\top}] \right) \\ &= \frac{N}{N-1} \mathbb{E}[XY^\top] - \frac{1}{N(N-1)} \left(N \cdot \mathbb{E}[XY^\top] + N(N-1) \cdot \mathbb{E}[X] \mathbb{E}[Y]^\top \right) \\ &= \mathbb{E}[XY^\top] - \mathbb{E}[X] \mathbb{E}[Y]^\top = \text{Cov}(X, Y).\end{aligned}$$

Given the samples $\{\Gamma^{(1)}, \dots, \Gamma^{(N)}\}$, we can then use the estimator above to get,

$$\begin{aligned}\widehat{\text{Cov}}(g(\Gamma), \nabla_\theta U_\theta(\Gamma)) &= \frac{1}{N-1} \sum_{i=1}^N g(\Gamma^{(i)}) \nabla_\theta U_\theta(\Gamma^{(i)})^\top - \frac{1}{N(N-1)} \left(\sum_{j=1}^N g(\Gamma^{(j)}) \right) \left(\sum_{k=1}^N \nabla_\theta U_\theta(\Gamma^{(k)})^\top \right)^\top \\ &= \frac{N}{N-1} \left[\hat{\mathbb{E}} \left[g(\Gamma) \nabla_\theta U_\theta(\Gamma)^\top \right] - \hat{\mathbb{E}}[g(\Gamma)] \hat{\mathbb{E}}[\nabla_\theta U_\theta(\Gamma)]^\top \right].\end{aligned}$$

The final Boltzmann estimator is thus given as,

$$\mathcal{E}(\Gamma^{(1)}, \dots, \Gamma^{(N)}) \stackrel{\text{def}}{=} \frac{N}{k_B T(N-1)} \left[\hat{\mathbb{E}}[g(\Gamma)] \hat{\mathbb{E}}[\nabla_{\theta} U_{\theta}(\Gamma)]^{\top} - \hat{\mathbb{E}}[g(\Gamma) \nabla_{\theta} U_{\theta}(\Gamma)^{\top}] \right].$$

□

We note that a similar estimator is obtained in [65] by differentiating through a reweighting scheme arising from thermodynamic perturbation theory. We have presented an alternative derivation that does not require reweighting.

A.2 Localized Boltzmann Estimator

We provide additional details on the Localized Boltzmann Estimator. Formally, define a neighborhood of n atoms $\mathcal{N} = \{x_1, x_2, \dots, x_n \mid x_i \in \mathbb{Z}, 1 \leq x_i \leq N \text{ for all } i = 1, 2, \dots, n\}$. The local state γ is defined as $\gamma = \{[r_{\mathcal{N}_1}; \dots; r_{\mathcal{N}_n}], [P_{\mathcal{N}_1}; \dots; P_{\mathcal{N}_n}]\}$. The local energy is then defined as $U_{\theta}(\gamma) = \sum_{i=1}^n U_{\theta}(\gamma_i)$, where $\gamma_i = \{r_{\mathcal{N}_i}, P_{\mathcal{N}_i}\}$ contains the position and momenta of the i^{th} atom in the local neighborhood. We can obtain this by noting that NNIPs first compute individual atomic energies before summing over all atoms to obtain the global energy. Finally, given N i.i.d. samples of local states $\gamma^{(1)}, \dots, \gamma^{(N)}$, where each $\gamma^{(i)}$ is extracted from a global state $\Gamma^{(i)} \sim P_{\theta}(\Gamma)$, we define the N -sample localized estimator of the Jacobian $\frac{\partial \mathbb{E}_{\gamma \sim P_{\theta}(\gamma)}[g(\gamma)]}{\partial \theta}$ as

$$\mathcal{E}(\gamma^{(1)}, \dots, \gamma^{(N)}) \stackrel{\text{def}}{=} \frac{N}{k_B T(N-1)} \left[\hat{\mathbb{E}}[g(\gamma)] \hat{\mathbb{E}}[\nabla_{\theta} U_{\theta}(\gamma)]^{\top} - \hat{\mathbb{E}}[g(\gamma) \cdot \nabla_{\theta} U_{\theta}(\gamma)^{\top}] \right] \quad (8)$$

The localized estimator follows from the original Boltzmann estimator due to the fact that as a subset of the larger Boltzmann-distributed system, any local neighborhood also obeys a Boltzmann-distribution. In practice, we extract multiple local neighborhoods from each global state to increase the sample size and state space coverage. See Supplementary Section A.6 for a description of the neighborhood extraction procedure used for the Water system.

A.3 StABIE Training Algorithm

We provide an algorithmic description of our StABIE-Training procedure. The algorithm proceeds in two main phases: simulation, which seeks out unstable regions of molecular phase space, and learning, which corrects the instability via supervision from the reference observables.

Algorithm 1 StABIE Training Procedure

```

1: Initialize:
2: Pre-trained Neural Network Potential  $U_\theta$ 
3: Reference energy and forces dataset  $\mathcal{D}_{\text{train}}$  and observables  $\{g_{\text{ref}}^{(i)}\}_{i=1}^N$ 
4: Simulation length  $t$ , number of parallel replicas  $R$ , minimum unstable threshold  $f_{\text{min}}$ ,
5: maximum unstable threshold  $f_{\text{max}}$ , energy and forces loss weight  $\lambda$ , learning rate  $\alpha$ 
6:
7:  $\bar{\Gamma}_{\text{curr}} \leftarrow \{\Gamma^{(1)}(0), \Gamma^{(2)}(0), \dots, \Gamma^{(R)}(0)\} \sim \mathcal{D}_{\text{train}}$ 
8: Current fraction of unstable replicas  $f_{\text{unst}} \leftarrow 0$ 
9: Total simulated time  $T_{f_i} \leftarrow 0, \forall i = 1, \dots, R$ 
10: Mark all replicas as active for simulation
11: repeat
12:   while  $f_{\text{unst}} < f_{\text{max}}$  do
13:     Simulate active replicas w/  $U_\theta$  for  $t$  steps starting from  $\bar{\Gamma}_{\text{curr}}$ 
14:      $T_{f_i} \leftarrow T_{f_i} + t, \forall i$  corresponding to stable replicas
15:      $\bar{\Gamma}_{\text{curr}} \leftarrow \{\Gamma^{(1)}(T_{f_1}), \Gamma^{(2)}(T_{f_2}), \dots, \Gamma^{(R)}(T_{f_R})\}$ 
16:     Update  $f_{\text{unst}}$  and mark unstable replicas inactive
17:   end while
18:
19:   //  $\bar{\Gamma}_{\text{curr}}$  now contains  $\{\Gamma^{(1)}(T_{f_1}), \Gamma^{(2)}(T_{f_2}), \dots, \Gamma^{(R)}(T_{f_R})\}$ , where  $T_{f_i}$ 's are per-replica total simulation times
20:   // At least  $f_{\text{max}}$  fraction of replicas are unstable at this point
21:
22:   while  $f_{\text{unst}} > f_{\text{min}}$  do
23:     Rewind all trajectories by  $t$  timesteps:  $\bar{\Gamma}_{\text{curr}} \leftarrow \{\Gamma^{(1)}(T_{f_1} - t), \dots, \Gamma^{(R)}(T_{f_R} - t)\}$ 
24:     Simulate all replicas w/  $U_\theta$  for  $t$  steps starting from  $\bar{\Gamma}_{\text{curr}}$ 
25:     Update  $f_{\text{unst}}$ 
26:     Compute observables  $\{\widehat{\mathbb{E}}_\Gamma[g^{(i)}(\Gamma)]\}_{i=1}^N$  over all length- $t$  trajectories
27:      $\mathcal{L}_{\text{obs}} \leftarrow \sum_{i=1}^N \|\widehat{\mathbb{E}}_\Gamma[g^{(i)}(\Gamma)] - g_{\text{ref}}^{(i)}\|^2$ 
28:      $\mathcal{L}_{\text{QM}} \leftarrow$  energy and forces loss of  $U_\theta$  on dataset  $\mathcal{D}_{\text{train}}$ 
29:      $\theta \leftarrow \theta - \alpha \cdot \nabla_\theta(\mathcal{L}_{\text{obs}} + \lambda\mathcal{L}_{\text{QM}})$  // Compute Boltzmann Estimator
30:   end while
31:   Mark stable replicas active, unstable replicas inactive for next simulation phase
32:   // At most  $f_{\text{min}}$  fraction of replicas are unstable at this point
33: until Convergence or maximum cycles reached

```

} **Simulation Phase**

} **Learning Phase**

A.4 Observables

We provide definitions and details of the observables considered in this work.

Distribution of Interatomic Distances. The distribution of interatomic distances serves as a low-dimensional description of 3D structure. For a configuration $r' \in \mathbb{R}^{N \times 3}$, it is defined as,

$$h(r) = \frac{1}{N(N-1)} \sum_{i=1}^N \sum_{j \neq i}^N \delta(r - \|r'_i - r'_j\|),$$

where δ is the Dirac-Delta function. Although the observable need not be differentiable with respect to r for our Boltzmann learning framework, we compute a differentiable version of $h(r)$ via Gaussian smearing as in [71] to facilitate comparison with differentiable simulation methods.

Radial Distribution Function. The radial distribution function (RDF) captures how density (relative to the bulk) varies as a function of distance from a reference particle, and thus characterizes the structural/thermodynamic properties of the system. The RDF is defined as,

$$RDF(r) = \frac{V}{N^2 4\pi r^2} h(r).$$

where V is the volume of the simulation domain, N is the number of particles, r is the radial distance from a reference particle, and $h(r)$ is a histogram of pairwise distances. As with $h(r)$, we use Gaussian smearing to make the RDF differentiable.

Velocity Autocorrelation Function. The velocity autocorrelation function (VACF) is an important dynamical observable. Many fundamental properties, such as the diffusion coefficient and vibrational spectra, are functions of this observable. Computing the VACF requires a window of consecutive simulation states to compute. The VACF at a given time lag Δt is given by,

$$VACF(\Delta t) = \frac{1}{S} \sum_{t_0} \sum_i \langle v_i(t_0), v_i(t_0 + \Delta t) \rangle,$$

where t_0 is an initial time, $v_i(t)$ is the velocity of the i^{th} atom at timestep t , $\langle \cdot, \cdot \rangle$ is an inner product, and S is the total number of samples considered given the summations over initial times and atoms. In this work, we compute the VACF over a window of 100 consecutive simulation timesteps, and normalize the values by the autocorrelation at $\Delta t = 0$ to restrict the range to $[0, 1]$.

Diffusivity Coefficient The diffusivity coefficient is a fundamental transport property with crucial implications on the performance of energy storage systems, among other applications. Related to the time-derivative of the mean squared displacement, the diffusivity coefficient is defined as,

$$D = \lim_{t \rightarrow \infty} \frac{1}{6t} \frac{1}{N} \sum_{i=1}^N |r_i(t) - r_i(0)|^2$$

, where $r_i(t)$ is the coordinate of the i^{th} particle at time t and N is the number of atoms considered. For the water system considered in this work, we measure the diffusivity of all 64 oxygen atoms.

A.5 Stability Criteria

We provide definitions and details on the stability criteria considered in this work.

Maximum Bond Length Deviation. Adapted from [23], the maximum bond length deviation metric captures unphysical bond stretching or collapse in small flexible molecules. According to this criterion, a simulation becomes unstable at time T if,

$$\max_{(i,j) \in \mathcal{B}} |(\|r_i(T) - r_j(T)\| - b_{i,j})| > \Delta,$$

where \mathcal{B} is the set of all bonds, i, j are the two endpoint atoms of the bond, and $b_{i,j}$ is the equilibrium bond length computed from the reference simulation. Following [23], we set $\Delta = 0.5A$ for final stability evaluation. However, we adopt a more conservative value of $\Delta = 0.25A$ during training in order to detect and correct instability earlier. We use this criterion for the MD17 and MD22 datasets.

Minimum Intermolecular Distance. The minimum intermolecular distance metric is used to detect unphysical coordination structures or collisions between molecules in the water system. According to this criterion, a simulation becomes unstable at time T if,

$$\min_{(i,j) \notin \mathcal{B}} \|r_i(T) - r_j(T)\| < \Delta,$$

where \mathcal{B} is the set of all bonds, and i, j are the endpoint indices of two non-bonded atoms. We set $\Delta = 1.2A$ to detect instability during training.

Radial Distribution Function Mean Absolute Error. The minimum intermolecular distance metric is appropriate at train-time to detect instability early before it cascades to the rest of the system. However, it is too sensitive to use for evaluation, as realistic simulation can still be achieved for some time after the occurrence of a highly localized instability. Therefore, following [23], we adopt an instability metric based on the radial distribution function, defined as,

$$\int_{r=0}^{\infty} \left\| RDF_{\text{ref}}(r) - \langle RDF^t(r) \rangle_{t=T}^{T+\tau} \right\| dr > \Delta,$$

where $\langle \cdot \rangle$ is the averaging operator, τ is a short time window, and Δ is the stability threshold. We use $\tau = 1$ ps and $\Delta = 3.0$ for water. The stability criterion is triggered if any of the three element-conditioned water RDFs (H-H, O-O, or H-O) exceeds the threshold.

Justification of Chosen Stability Thresholds. Following [23], we choose stability thresholds such that a realistic, high-fidelity simulation at the chosen temperature would virtually never cross the threshold. This means that if a simulation does cross the threshold, this is indicative of catastrophic failure. Thresholds are set more conservatively during training in order to facilitate early detection of potential collapse. Figure 7 shows the distribution of values of the stability criterion over high-fidelity reference simulations for the three systems considered in this work, along with thresholds chosen to denote instability for training and evaluation.

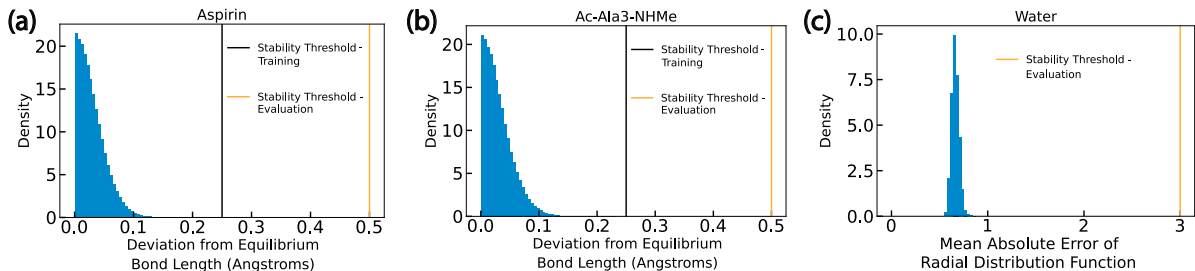


Figure 7: Distribution of stability criterion over reference simulations. Instability thresholds are chosen to be very relaxed, such that crossing of the threshold signifies catastrophic, unrecoverable instability.

A.6 Architecture and Training Details

We provide details on the model architectures and training procedures used in this work. MD simulations and NNIPs are written in the PyTorch framework and are built upon the MDsim [23] and Atomic Simulation Environment [40] packages. All training is performed on a single NVIDIA A100 GPU.

Table 1 provides details on the NNIP architectures. r_{max} is the cutoff distance used to construct the radius graph. l_{max} denotes the level of E(3) equivariance used in the network.

	Symmetry Principle	Parameter Count	r_{max} (Å)	l_{max}
SchNet [58]	E(3)-invariant	0.12M	5.0	-
NequIP [5]	E(3)-equivariant	0.12M	5.0	1
GemNet-T [24]	SE(3)-equivariant	1.89M	5.0	-

Table 1: NNIP Architecture Details.

For energy and forces pre-training, we follow the protocols in [23]. In order to isolate the effect of observable-based learning, we begin StABIE Training only after pre-training has fully converged (that is, when \mathcal{L}_{QM} has reached a plateau). This means that any improvements in stability or accuracy as a result of StABIE Training can be attributed to the learning signal from the reference observable, as opposed to the regularization from the QM energy and forces data.

We include relevant settings used for StABIE Training in Table 2. α is the learning rate, λ is the strength of energy and forces regularization, t is the number of simulation timesteps per epoch, and R is the number of parallel replicas. We note that in practice, we compute the outer products and empirical means in the Boltzmann estimator in batched fashion. Thus, to limit memory usage, we compute $\frac{N}{B}$ separate Boltzmann estimators from minibatches of $B < N$ states and subsequently average them to produce a final estimator.

	NNIP	Stability Criterion, Threshold	Training Observable	Estimator Type	α	λ	t	R	B
Aspirin	SchNet	Bond Len. Dev., 0.25 Å	$h(r)$	Global	0.001	10	2000	128	40
Ac-Ala3-NHMe	NequIP	Bond Len. Dev., 0.25 Å	$h(r)$	Global	0.001	10	2000	128	40
Water	GemNet-T	IMD, 1.2 Å	O-H Bond Length	Local	0.003	0	1000	8	4

Table 2: StABIE Training Settings.

Details on Local Neighborhood Sampling Scheme for Water. For water training, from each sampled global state we consider all possible local neighborhoods containing a single water molecule. Since instability is highly localized, the majority of local neighborhoods are stable, leading to an imbalance in the sampled states. To provide more informative samples for optimization, we assign the individual sampled molecules to one of 100 bins based on their deviation from the equilibrium O-H bond length. Then, we choose a fixed number (in this case 5) molecules from each bin from which to compute the final localized estimator.

Wall Clock Time of StABIE Training. In Table 3, we provide the total wall clock time spent on QM pre-training, as well as the subsequent StABIE Training. All runtimes were measured on an NVIDIA A100 GPU. We note that especially for Ac-Ala3-NHMe and Water, StABIE Training incurs a relatively small marginal computational cost beyond that of QM pre-training.

	QM pre-training	StABIE Training
Aspirin	2	4
Ac-Ala3-NHMe	16	4.7
Water	31	3.5

Table 3: Wall clock time, in hours, of QM pre-training and StABIE Training.

A.7 Simulation Details

We provide MD simulation details in Table 4. All systems considered in this work are simulated with a Nose-Hoover thermostat. All simulation parameters are chosen to be consistent with prior literature [18, 17, 23].

	Temperature (K)	Nose-Hoover Effective Mass (cm^{-1})	Timestep (fs)	Periodic Boundary Conditions
Aspirin	500	2000	0.5	No
Ac-Ala3-NHMe	500	2000	0.5	No
Water	300	2000	1	Yes

Table 4: Simulation Settings.

A.8 Evaluation Details

We provide further details on the protocol used to evaluate the NNIPs considered in this work. Our evaluation protocol is centered around MD simulations. To facilitate direct comparison between StABIE-trained NNIPs and those trained only on energy and forces reference data, for a given molecular system we perform MD simulations starting from the same initial configurations for all models. We choose the number of

parallel replicas and total simulation time on a per-system basis so as to saturate GPU memory usage while remaining within a reasonable computational budget. Simulation conditions are the same as described in Section A.7 except for the temperature generalization experiment (Section 3.2), in which the temperature of simulation is varied. Table 5 summarizes the relevant evaluation parameters for each system.

	Num. Parallel Replicas	Max. Simulation Time (ps)	Stability Criterion, Threshold
Aspirin	256	300	Bond Length Deviation, 0.5 Å
Ac-Ala3-NHMe	48	300	Bond Length Deviation, 0.5 Å
Water	10	200	RDF MAE, 3.0

Table 5: StABIE Evaluation Settings.

A.9 Temperature-Reweighting of Observables

We provide further details on the reweighting process used to estimate the reference distribution of inter-atomic distances at 350K and 700K.

Under the canonical ensemble, microstates follow a Boltzmann distribution $P_\theta(\Gamma) \stackrel{\text{def}}{=} \frac{\exp\left(-\frac{1}{k_B T} \mathcal{H}_\theta(\Gamma)\right)}{C(\theta)}$. Consider states $\Gamma^{(1)}, \dots, \Gamma^{(N)}$ sampled at temperature T_1 . Define a reweighting factor for each sample as follows,

$$w_i = \frac{\frac{P_\theta(\Gamma; T_1)}{P_\theta(\Gamma; T_2)}}{\sum_{i=1}^N \frac{P_\theta(\Gamma^i; T_1)}{P_\theta(\Gamma^i; T_2)}} = \frac{\exp\left(-\frac{\mathcal{H}_\theta(\Gamma^i)}{k_B} \left(\frac{1}{T_2} - \frac{1}{T_1}\right)\right)}{\sum_{i=1}^N \exp\left(-\frac{\mathcal{H}_\theta(\Gamma^i)}{k_B} \left(\frac{1}{T_2} - \frac{1}{T_1}\right)\right)}.$$

We can then compute a reweighted Monte Carlo estimate of the observable at T_2 as follows [65],

$$g_{true, T_2} = \sum_{i=1}^N w_i g(\Gamma^{(i)})$$

The statistical error of the reweighted Monte Carlo estimate is captured by the effective sample size, $N_{eff} \approx e^{-\sum_{i=1}^N w_i \ln(w_i)}$ [13]. A small effective sample size indicates that a few samples with high weights dominate the average; this occurs for large differences between T_1 and T_2 . To select lower and upper temperatures at which to perform the temperature generalization experiment, we set a minimum $N_{eff} = 1000$, leading us to choose 350K and 700K (Supplemental Figure 8).

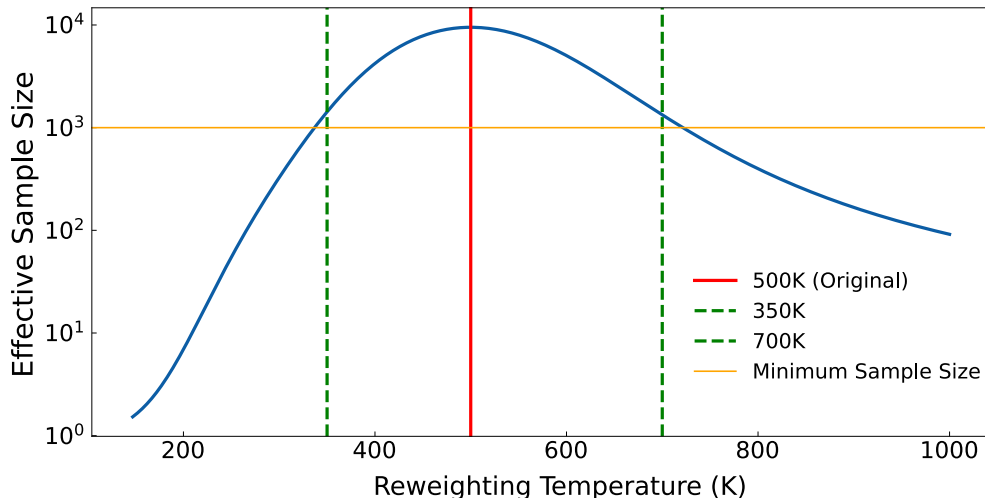


Figure 8: Boltzmann-reweighting of aspirin samples. The effective sample size (N_{eff}) as a function of reweighting temperature for aspirin dataset. N_{eff} is maximized when the reweighting temperature is equal to the original temperature (500K). Using a minimum sample size of 1000, we choose upper and lower temperatures of 700K and 350K at which to perform temperature generalization experiments.

A.10 Analysis of Energy and Forces Errors

We study the effect of two hyperparameters of StABIE Training, the learning rate α and the strength of QM regularization λ , on the energy and forces errors of a SchNet NNIP on a held-out test set of aspirin structures. We perform StABIE Training as described in Section 2 for learning rates ranging from 10^{-5} to 10^{-3} and QM regularization coefficients ranging from 10^0 to 10^2 . We perform evaluation of each trained model via MD simulation of 256 parallel replicas at 500K.

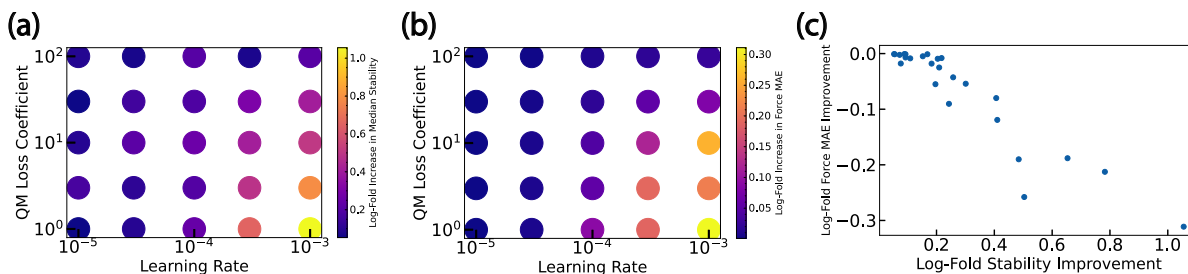


Figure 9: Effect of training hyperparameters on stability and force error improvements. (a) Models trained with higher learning rate and lower QM loss coefficient achieve better stability gains relative to a baseline model trained only on QM reference data. (b) Models trained with higher learning rate and lower QM loss coefficient incur higher increases in force mean absolute error (MAE) on a held-out test dataset relative to the baseline model. (c) A Pareto frontier of Stability vs Force MAE arises. Some choices of learning rate and loss coefficient are Pareto-suboptimal, while choosing others moves along the Pareto frontier.

Training runs with high learning rate and low QM loss coefficient achieve greater improvements in stable simulation time relative to a baseline model trained only on QM reference data (Figure 9a). However, these training runs also incur a greater increase in the Mean Absolute Error (MAE) of force prediction on a held out test dataset (Figure 9b). Due to training on a single structural observable, the observable-

matching component of the StABIE objective is ill-posed: a NNIP which collapses simulations onto a sparse set of states exactly matching the reference observable would globally minimize the observable-matching loss and yield indefinitely stable simulations, while incurring a large QM/force error. As the learning rate of the StABIE Training procedure is increased, the optimization is increasingly pushed towards this degenerate mode. Increasing the weight of the QM objective counteracts this tendency. Consequently, a Pareto frontier arises between stability and force prediction accuracy (Figure 9c). Some settings of learning rate and QM loss coefficient are Pareto suboptimal, while choosing among the remaining combinations causes one to move along the frontier. Incorporating additional training observables, particularly those which are dynamical in nature (e.g velocity autocorrelation functions), could counteract the degeneracy and push the Pareto frontier outwards.

Finally, we note that the observed energy MAE increase on aspirin for our chosen combination of learning rate ($\alpha = 0.001$) and loss coefficient ($\lambda = 10$) is from 0.87 to 1.4 kcal mol⁻¹, while DFT error for energies on MD17 can be as high as 2.3 kcal mol⁻¹ [20]. Thus, some of the error in the NNIP predictions could be attributable to inaccuracies in the underlying DFT data.

A.11 Effect of Simulation Timestep on Stability

To demonstrate that the instability problem in NNIPs is not simply due to an inappropriate choice of simulation timestep, we perform simulations at various timesteps for each pair of system and model (Figure 10).

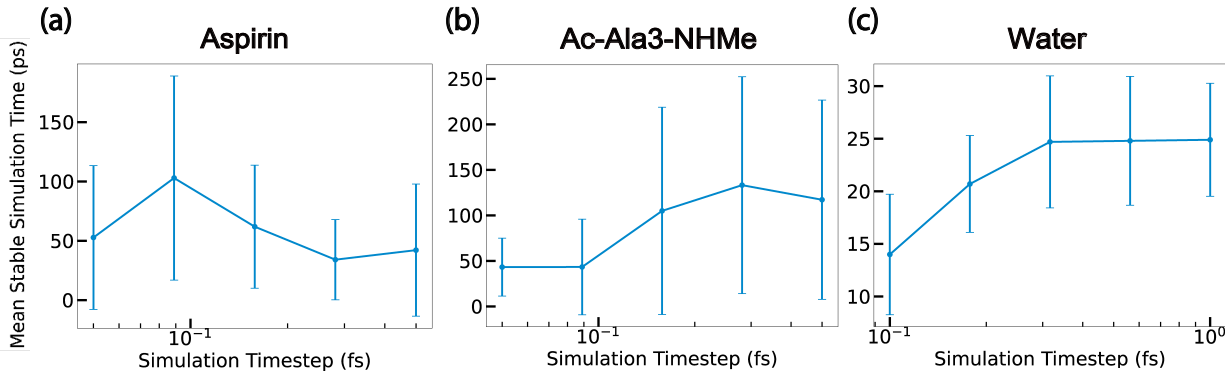


Figure 10: Effect of timestep on simulation stability. Reducing the timestep does not reliably lead to an improvement in stability, and can sometimes worsen stability.

We observe that stability does not necessarily improve as the timestep is reduced. In fact, for some systems, stability seems to consistently decrease as the timestep is reduced. Similar behavior has been observed in neural network based solvers for ordinary differential equations [38].

A.12 Velocity Autocorrelation Function of Aspirin

We show the aspirin velocity autocorrelation function (VACF) corresponding to the trajectory with the median stability improvement between conventional and StABIE Training. A StABIE-trained model produces a similar VACF relative to a conventionally trained model. This suggests that the StABIE procedure does

not significantly interfere with dynamic properties of the simulation, despite only training with a structural observable ($h(r)$).

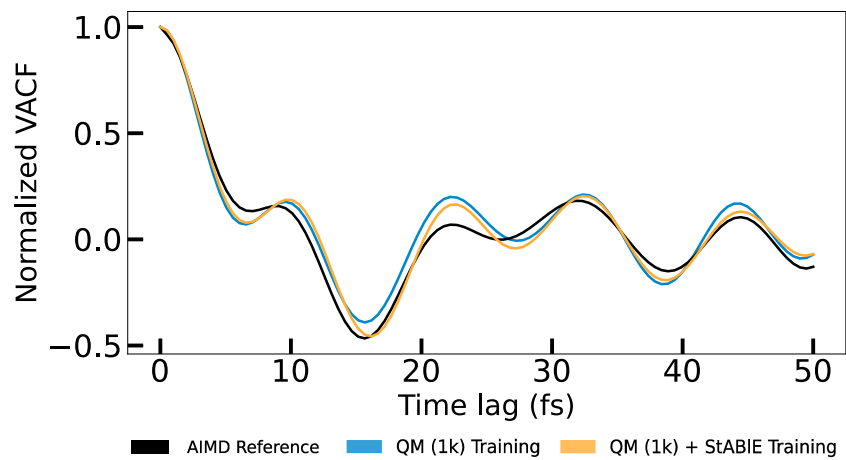


Figure 11: Velocity autocorrelation function of aspirin.